2022-12-01

Modulation of Non-diffracting Hermite Gaussian Beams and Nonlinear Optical Microscopy for Nanoscale Sulfur Imaging

Gilberto Navarro
University of Texas at El Paso

MODULATION OF NON-DIFFRACTING HERMITE GAUSSIAN BEAMS

AND NONLINEAR OPTICAL MICROSCOPY FOR

NANOSCALE SULFUR IMAGING

GILBERTO III NAVARRO

Master's Program in Physics

APPROVED:

Chunqiang Li, Ph.D., Chair

Ahmed El-Gendy, Ph.D.

Thomas Boland, Ph.D.

Stephen L. Crites, Jr., Ph.D.
Dean of the Graduate School

Dedication

I'd like to dedicate this to my parents. The unconditional support that both my parents have shown me has been a blessing. I am forever grateful.

MODULATION OF NON-DIFFRACTING HERMITE GAUSSIAN BEAMS AND NONLINEAR OPTICAL MICROSCOPY FOR NANOSCALE SULFUR IMAGING

by

GILBERTO III NAVARRO, B.S.

THESIS

Presented to the Faculty of the Graduate School of

The University of Texas at El Paso

in Partial Fulfillment

of the Requirements

for the Degree of

MASTER OF SCIENCE

Department of Physics

THE UNIVERSITY OF TEXAS AT EL PASO

December 2022

Abstract

Hermite Gaussian beams are the solutions of the scalar paraxial wave equation in Cartesian coordinates. A method was developed to modulate the intensity profile of non-diffracting Hermite Gaussian (HG) beams. The original HG beam's intensity profile consists of high intense corner lobes and low intense central lobes which is not ideal for structured illumination in light-field microscopy. The modulated HG beams were generated by multiplying the original HG's beam envelope by a super-Gaussian envelope to modify the intensity profile to attain equal intensity lobes. The propagation of the original HG beam and modulated HG beam were compared to determine that the non-diffracting properties of the modulated HG beam were held.

Two-photon absorption (TPA) is a nonlinear optical process in which the absorption coefficient depends on the optical intensity. In the process of two-photon absorption, an atom makes a transition from its ground state to an excited state by the simultaneous ($\sim$ 1 fs) absorption of two photons. In the second project, two-photon microscopy was used to detect the root uptake and determine the biodistribution of nanoscale sulfur. Characterization of pristine, stearic acid coated, and bulk sulfur was done to determine their fluorescent signal properties. Tomatoes that were grown in nano-sulfur treated soils to enhance crop nutrition and suppress disease, were imagined under the two-photon microscope to detect the root uptake of the nanoscale sulfur.

Table of Contents

List of Figures

Chapter 1: Light-Field Microscopy for Fast 3D Imaging

3D Fluorescence Imaging

Achieving high-speed 3D fluorescence imaging is an important technological development area for studying fast molecular and cellular processes *in vivo* in biomedical research. Conventional laser scanning microscopes achieve volumetric imaging via point-by-point scanning of the interested volume (Figure 1(a)), which is a bottleneck for imaging fast biological processes such as neural signaling which happens in milliseconds. Light-sheet microscopy achieves plane-by-plane imaging by using a camera as the light detector. However, it still needs scanning in the z-direction, i.e., depth to obtain volumetric information (Figure 1(b)).

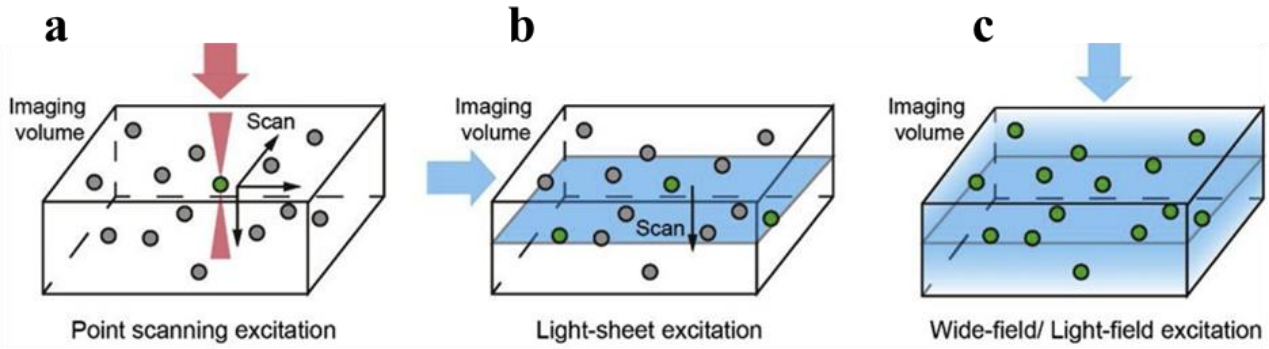

Figure 1: Comparison of 3D fluorescence imaging methods

Light-field microscopy (LFM) is a new direction of 3D imaging (Figure 1(c)), which can acquire volumetric images in one snapshot by placing a microlens array (MLA) in front of the detection camera, thus enabling kHz imaging speed with demonstrated success in live animal neural imaging.

Light-Field Microscopy

Let us start by understanding the plenoptic function L(x,y,z,$\theta, \emptyset$) that expresses the image of a scene from any possible viewing position at any viewing angle at any point in time. Since rays in space can be parametrized by three coordinates and two angles then the plenoptic function is 5D. Since the radiance of a ray remains constant from point to point along its length, we gather no additional information. In this case, the information becomes redundant. The redundant information is exactly one dimension, leaving us with a 4D function historically called the light field L(x,y,θ,∅)) (Levoy M. & Zhang Z., 2009).

In Levoy's 2009 paper "Recording and controlling the 4D light field in a microscope using microlens arrays" he parametrizes the 4D light field as rays by their intersection with two planes. A simple way to think about a two-plane light field is as a collection of perspective views of the *st* plane, each taken from an observer position on the *uv* plane (Levoy M. & Zhang Z., 2009). In the case of the light field microscope, one pixel (s, t) on the camera behind one certain micro-lens (u, v) in a micro lens array (MLA) receives light ray whose positional and directional in-formation can both be inferred from two intersection points (u, v) and (s, t).

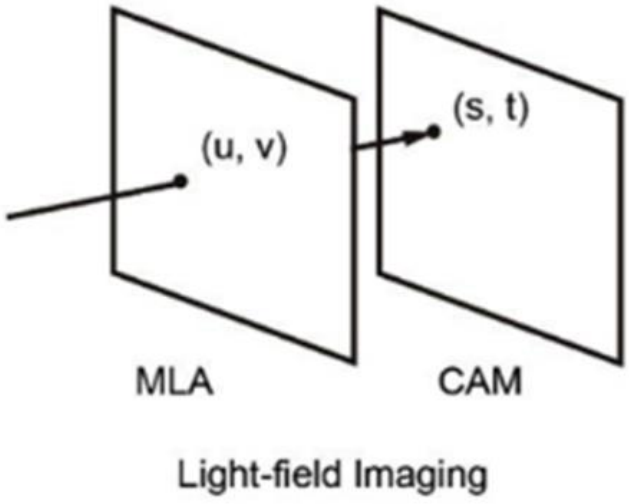

Figure 2: MLAs are used in the intermediate image plane to multiplex spatial (s, t) and directional (u, v) information on a single image sensor.

Light-field microscopy (LFM) captures both the 2D spatial and 2D angular information of the incident light all at once. Meaning that the recorded 2D sub-images contain 4D information (x,y,θ,∅). Where x and y are the spatial coordinates and θ and ∅ are the angles of the incident light rays reaching the camera sensors. With the gathered 4D information, a computational reconstruction can be done to obtain a 3D volumetric image using a reconstruction algorithm based on geometric optics, tracing light rays to determine the spatial coordinates and the angles. However, this approach is not ideal for microscopic imaging due to the high numerical apertures of optical elements. Therefore, the geometric optical approximation is invalid. New 3D deconvolution algorithms for LFM based on wave optics have been developed to achieve higher spatial resolution in all three dimensions (x,y,z).

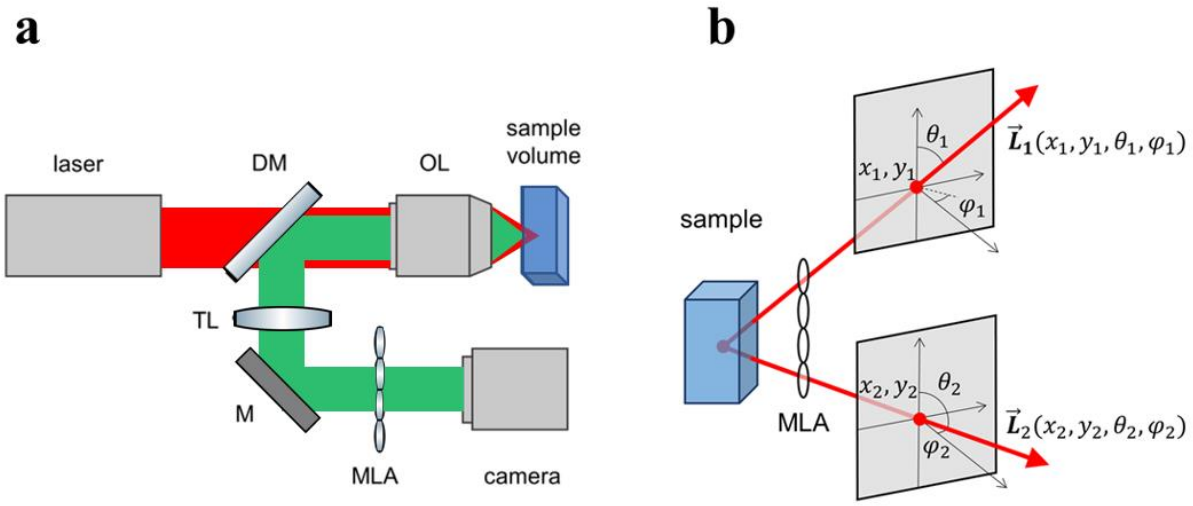

Figure 3: (a) Light-field microscope set up. DM: dichroic mirror, OL: objective lens, TL: tube lens, MLA: microlens array, RL: relay lens. (Green: laser beam, red: fluorescence signal) (b) 4D information (x, y, θ , φ) in raw LFM image.

LFM Detection Paths

The conventional light-field microscope consists of a microlens array (MLA) placed at the native image plane (NIP) and the imaging sensor is placed at the back focal plane of the MLA to record the 4D light-field information (Figure 4(a)). The conventional setup alleviates the tradeoff between spatial and angular information. However, it has limitations that restrict it from wave-optics models that allow for the reconstruction of densely aliased high-spatial frequencies through point-spread function (PSF) deconvolution (Guo et al., 2019). Due to its prohibitive reconstruction artifacts and considerably slow 3D reconstruction, which makes it impractical for rapid observations of the functional data, it sets its limits for the post-processing of imaging data.

To improve the current LFM , a Fourier light-field microscopy (FLFM) technique was proposed to achieve high-quality imaging and rapid light-field reconstruction. In FLFM, the MLA is placed at a certain distance behind the NIP (Figure 4(b)). Now the imaging plane (sensor) is conjugated to the back aperture of the objective lens, which improves the lateral resolution (x, y) with the trade-off of less angular resolution (θ, φ) leading to reduced imaging depth in the axial dimension. Hence, this high-resolution LFM is suitable for 3D cellular and subcellular imaging (Li et al., 2019).

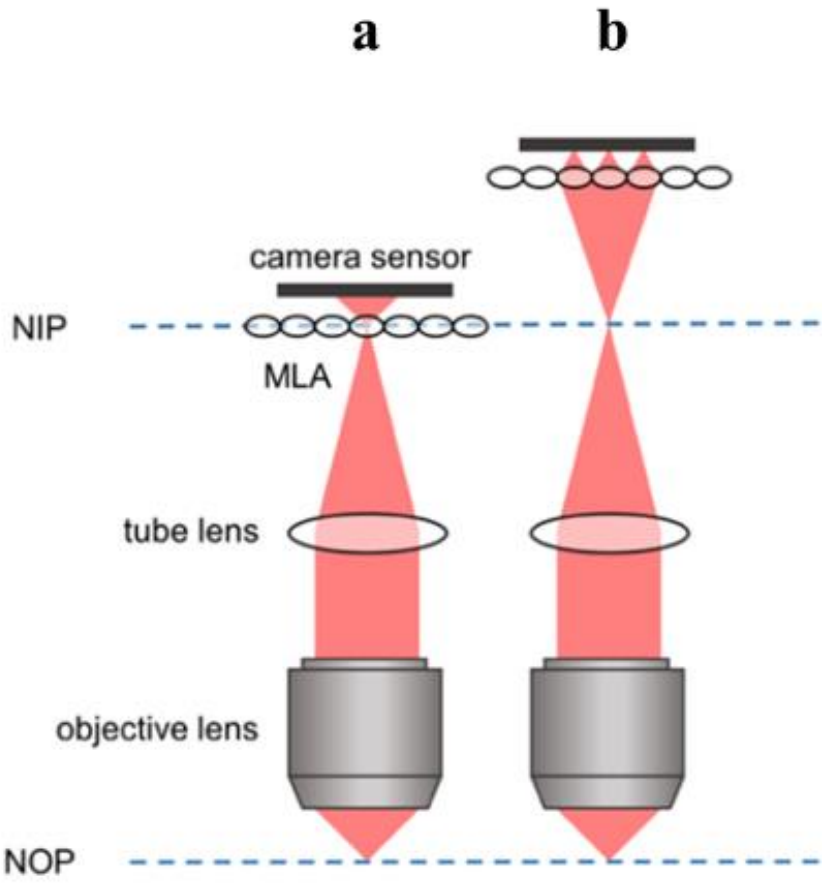

Figure 4: Illustration of the detection path: (a) LFM technique, (b) FLFM technique. NIP: native image plane, NOP: native object plane.

Point Spread Function

In the 1800s, Ernst Abbe demonstrated that resolution in the light microscope is limited by diffraction. This results in a blurry appearance of the captured image. In a specific mathematical description, the image is a convolution of the actual object with the so-called point spread function (PSF) of the optical system. The term convolution ($\otimes$) describes the physical phenomenon of the overlap of the PSFs and can be described as the imaging formula

$$I_{Image} = I_{Actual} \otimes \text{PSF} \quad (1)$$

The PSF describes the response of an optical system to a point source or object due to the diffraction limit. It gives us an understanding of the imaging performance, such as the theoretical resolution limit and the optical sectioning capacity (Li et al., 2018). A careful evaluation of the realistic PSF in optical microscopy can improve the deconvolution performance and support the optimization of the microscope. Thus, allowing for the precise reconstruction of biological structures.

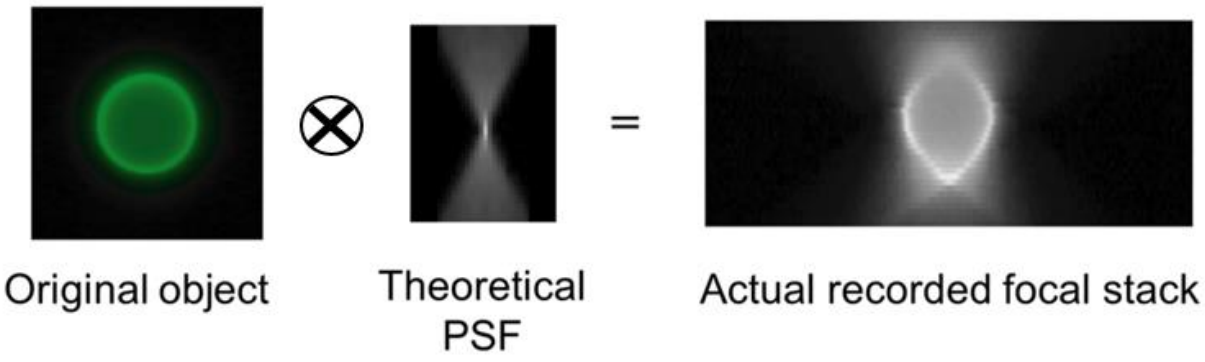

Figure 5: The microscope optics convolve each point source with the PSF

Deconvolution Microscopy

Deconvolution microscopy is an image-processing method that computationally reverses the effects of the blurry image that was captured. This method consists of two types of deconvolutions, deblurring and image restoration. Deblurring is a faster approach to reducing the blur in the image, but it tends to have its disadvantages (Goodwin, 2014). Since deblurring is a subtractive process, the signal is lost, and the noise is increased. Resulting in a reduced signal to noise ratio of the resulting image. Also, the results produced are generally not linear. As computational advances have been made these deblurring algorithms have become unnecessary.

Image restoration focuses back on to the imaging formula Eq.(1). By taking a close measure of the "blurred" image (I_{Image})and the PSF, the inversion solution method can be applied to derive the best estimate of the actual image (I_{Actual}). The inversion solution is a method

in which the Fourier transform (FT) transforms Eq.(1) into frequency space. In frequency space, the convolution becomes less complex and simply becomes multiplication (Goodwin, 2014)as

$$FT(I_{Image}) = FT(I_{Actual}) \times \mathrm{FT(PSF)} \quad (2)$$

Once rearranged to get $\mathrm{FT}(I_{Actual})$, the inverse Fourier transform can be applied to solve for I_{Actual}. Overall, the combination of innovative optical approaches and computational methods is pushing light-field microscopy toward in vivo observation of fast dynamic biological processes.

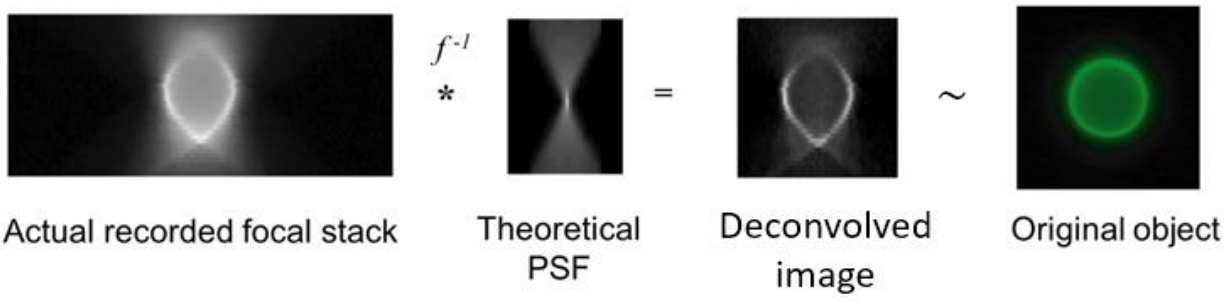

Figure 6: The inversion solution method can be applied to derive the best estimate of the actual image

Structured Illumination

In recent years there have been a number of exciting imaging technique developments collectively termed super-resolution microscopy. Super-resolution microscopy allows for the observation of fluorescent samples at resolutions going beyond the diffracting limit. Structured illumination microscopy (SIM) is one of the strategies applied to go beyond the diffracting limit and attain super-resolution.

SIM relies on a laser based widefield microscopy set-up with a known structured illumination pattern. The structured illumination pattern illuminates the sample that has an unknown pattern structure. This superimposition of illumination structure and sample structure generates a so-called Moiré effect (Figure 7(a)). What we see is that the fringe patterns that are observed are much lower frequency, they are much coarser. Fine structure information is encoded in coarse Moiré fridges. Where we can extrapolate spatial features of the unknown sample. This provides a way of getting high-frequency information that would be beyond what the objective lens could see and putting it back into the objective lens and capturing that information. By acquiring different images prepared from three phases at 120-degree orientations, and by mathematically deconvolving the interference signal, a super-resolution that contains twice the spatial resolution image is obtained.

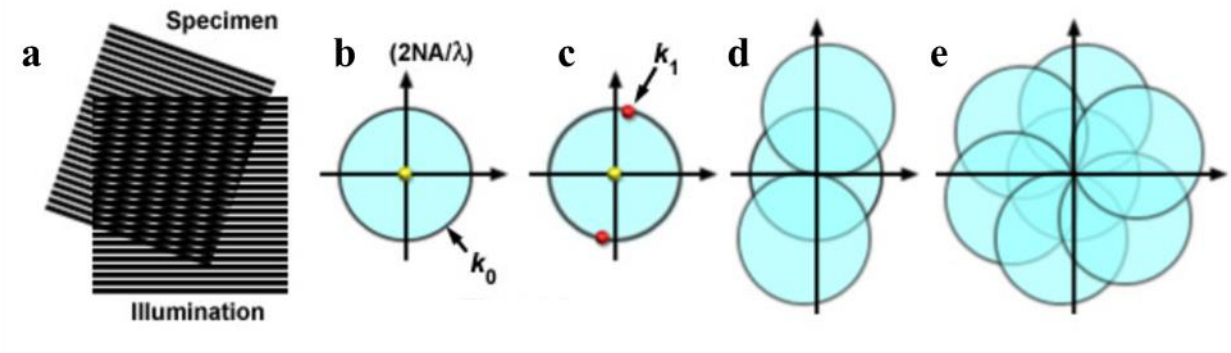

Figure 7: a) Moiré fringes generated by two overlapping patterns b) Maximum observable spatial frequency $k_0 = 2NA/\lambda_{em}$ c) Structured illumination of frequency k1 , where the zeroth (yellow) and first order (red) are the diffraction components from Moiré fringes. d) Two new offset frequency images that contain higher spatial frequencies that are not observed using a conventional microscope. e) A set of images that were prepared from rotating the Moiré pattern at 120-degree orientations to obtain twice the spatial resolution. (Gustafsson et al., n.d.)

Innovative Light-Field Microscope

With the current developments in imaging techniques to increase resolution described in the sections above, light-field microscopy can be applied to the imaging of biological tissues, such as the brain. One major obstacle to LFM and more general fluorescence microscopy for in vivo imaging is the penetration depth into tissue due to scattering. The innovative approach of our LFM is to overcome this obstacle by implementing structured non-diffracting beams into light-field microscopy to improve the imaging volume. The advantages of using a non-diffracting beam over a conventional gaussian beam include long non-diffracting length and recovery of beam spatial profile after scattering, also known as the beam's self-healing property. In this case, a Hermite Gaussian (HG) beam was proposed to be used in the light-field microscope. Due to its structured illumination pattern and non-diffracting properties, it is ideal to

utilize HG beams for 3D structured illumination in light-field microscopy to achieve deeper penetration and to overcome tissue scattering. Also, two-photon microscopy uses IR lasers for excitation, which has a much less scattering effect than visible light (Denk et al., 1990).

There are two objectives applied to the microscope. Objective 1 will use the original objective lens as the excitation and detection objective (Figure 8). The structured illumination pattern is in the x-y plane. A spatial light modulator will be added to convert conventional Gaussian laser beams into HG beams, only making a minimal adjustment to the current light-field microscope setup. Objective 2 will add an illumination objective lens in the orthogonal direction to the original objective, and the HG beams are delivered to the sample from this side objective. The advantage of this approach is that the structured illumination pattern has a z-component, which will help to improve the spatial resolution in the z-dimension.

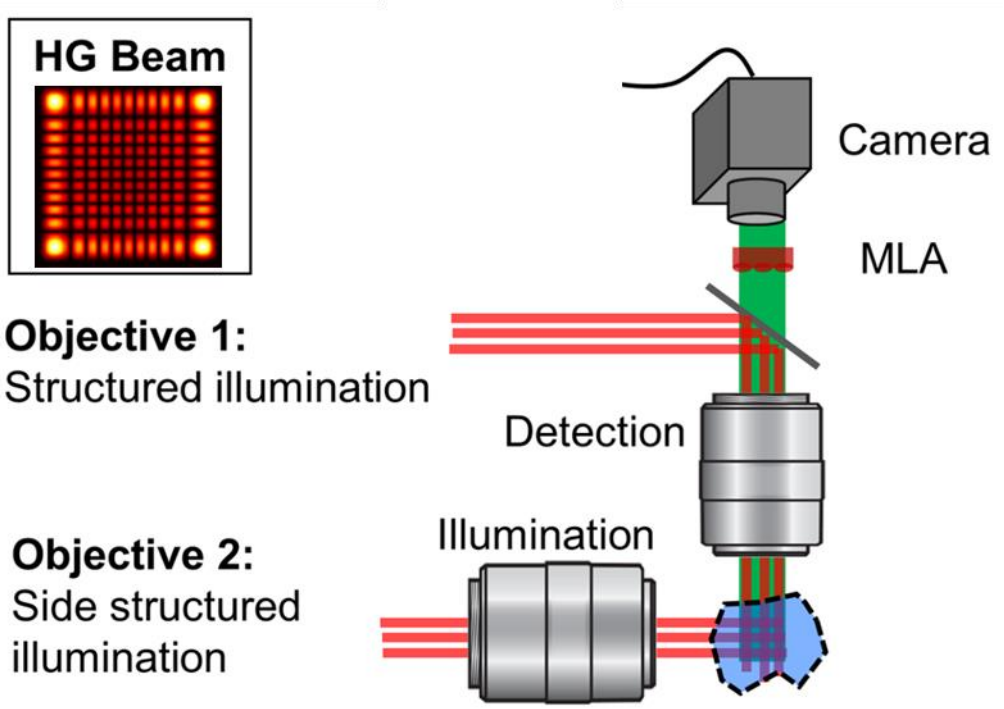

Figure 8: Schematic of innovative light-field microscope

Non-Diffracting Beams

In optics and particularly in laser physics, laser beams often occur in the form of Gaussian beams, which are named after the mathematician and physicist Johann Carl Friedrich Gauss (Paschotta 2008). The transverse profile of the optical intensity of the beam with an optical power P can be described with a Gaussian function:

$$I(r,z) = \frac{P}{\pi w(z)^2/2} \exp\left(-2\frac{r^2}{w(z)^2}\right) \quad (3)$$

Here, the beam radius w(z) is the distance from the beam axis and $r = (x^2 + y^2)^{1/2}$ is the transverse radial coordinate. The Gaussian beam would be considered a diffracting beam. As it travels through a short distance in space its intensity profile begins to diverge significantly due to the basic phenomena of diffraction. An example of a non-diffracting beam would be an Airy beam (Figure 9). The spatial Fourier spectrum of 1D Airy beam is given by the function:

$$\phi_0(k) = \exp(-ak^2)\exp\left(\frac{i}{3}(k^3 - 3a^2k - ia^3)\right) \quad (4)$$

where k is the normalized wave vector, and a is a decay factor determining Airy side lobes (Siviloglou & Christodoulides, 2007).

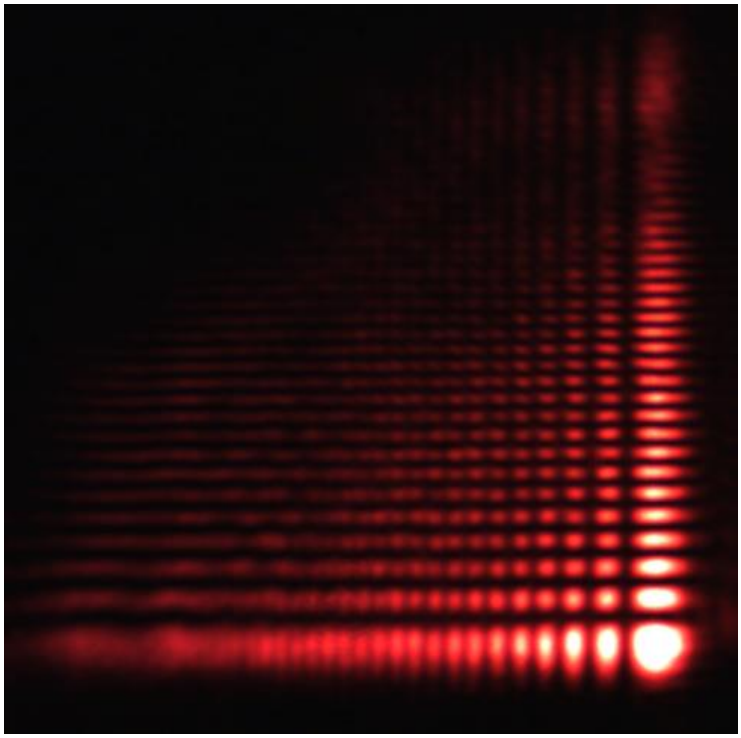

Figure 9: 2D Airy Beam

When a beam is described as non-diffracting caution should be taken to not ascribe the non-diffracting behavior of the center lobe to the individual photons. This behavior corresponds to the center lobe of the beam, and only over a short distance, at the sacrifice of the outer beam features. In the case of the Airy beam, it would be the outer lobes (Paez, 2019).Due to the Airy beam's non-diffracting, self-healing, and accelerating properties, it could greatly improve imaging depth in fluorescence microscopy by overcoming tissue scattering. In practice the limits to the non-diffraction aspects of these beams are the available power and aperture. However, even the limited non-diffraction length just has to be longer than the spatial features we require, at minimum 85 μm, ideally 100 μm (Vettenburg et al., 2014).

Hermite-Gaussian (HG) beams are part of the family of non-diffracting beams. The unique feature is HG beams possess symmetric patterns in Cartesian coordinates (x & y) designated as TEM_{lm} where l and m refer to the mode numbers in x & y dimensions respectively (Figure 10). Therefore, it is ideal to utilize HG beams for 3D structured illumination in light-field microscopy to achieve deeper penetration and to overcome tissue scattering.

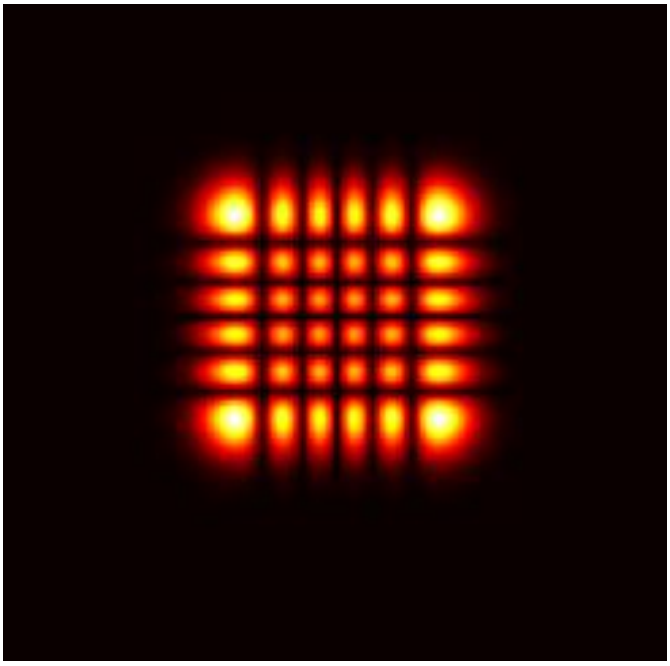

Figure 10: HG_{55} Beam

Hermite Gaussian Beam

Hermite Gaussian beams are the solutions of the scalar paraxial wave equation in Cartesian coordinates. Their complex amplitude is expressed at the waist plane z = 0 (near field), as

$$HG_{l,m}(x: y; w_o) = H_l\left(\frac{\sqrt{2}}{w(z)}x\right) H_m\left(\frac{\sqrt{2}}{w(z)}y\right) \exp\left(-\frac{r^2}{w(z)^2}\right), \quad (5)$$

where H_n (n = l, m) is the *n*th-order Hermite polynomial, $w_{(z)}$ is the beam waist, and just like the gaussian beam, $r = (x^2 + y^2)^{1/2}$ is the transverse radial coordinate. The indices l and m determine the shape of the Hermite Gaussian beam intensity profile in the x and y direction. The intensity distribution of such a mode has *l* nodes in the horizontal direction and *m* nodes in the vertical

direction (Figure 11). For $l = m = 0$, a Gaussian beam is obtained. This mode is called the *fundamental mode* or *axial mode*, and it has the highest beam quality with an M^2 factor of 1. Other Hermite–Gaussian modes with indices l and m have an M^2 factor of $(1 + 2\,l)$ in the x direction, and $(1 + 2\,m)$ in the y direction (Paschotta, 2004). The different HG modes can be numerically simulated from using Eq. (5). HG beam is known as a self-similar beam, it retains its shape during propagation. Therefore, its Fourier Transform (FT) also exhibits the transverse energy distribution similar to HG beams given by Eq. (5), and here we utilized this Fourier method for the generation of high order HG beams. The intensity profile at the focal plane (z = 0) can be derived via the Fraunhofer diffraction approximation utilizing the two-dimensional (2D) Fourier transform in Cartesian coordinates (Meena & Singh, 2021). The 2D Fourier transform of Eq.(12) is given by

$$\mathrm{FT}\{\mathrm{HG}(x,y)\} = \iint_{-\infty}^{\infty} HG_{l,m}(x,y) \times \exp\left[j2\pi\left(f_x x + f_y y\right)dxdy\right] \tag{6}$$

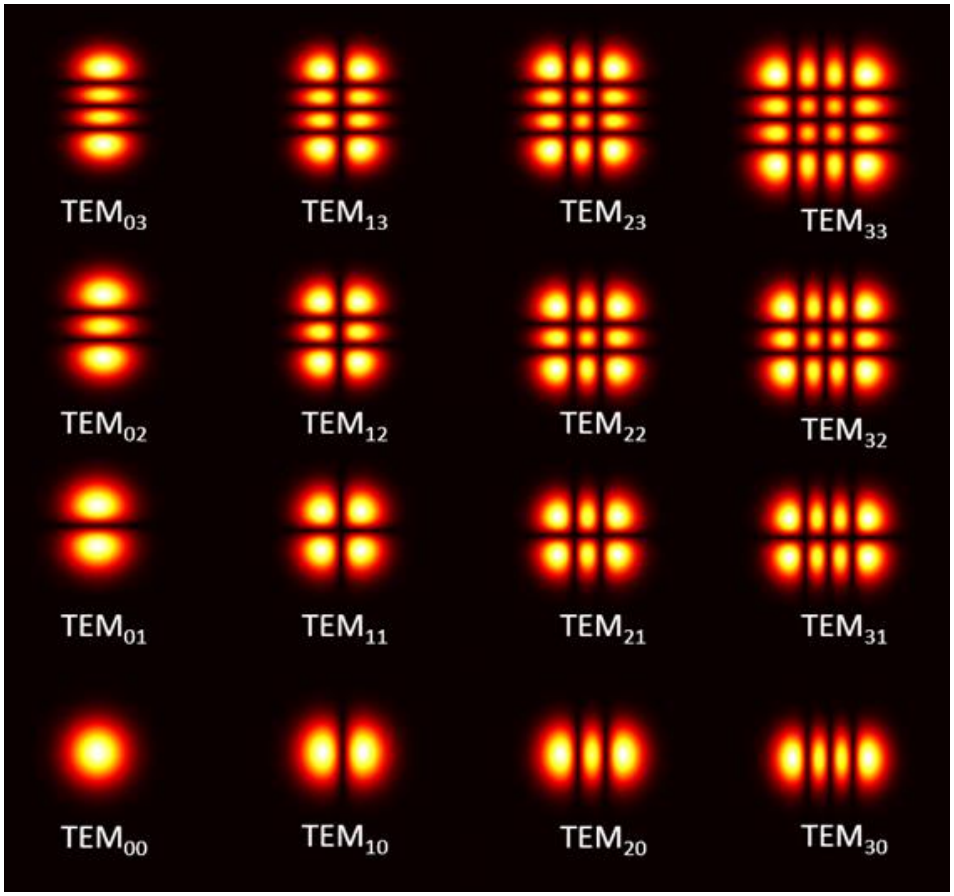

Figure 11: HG intensity profiles of lower-order modes, beginning with TEM00 (Lower left corner) and going up to TEM33 (Upper right corner).

where, f_x and f_y are the spatial frequencies along x and y directions.

Although the intensity profiles of the lower-order modes don't differ intensively from lobe to lobe (Figure 12(a)), once we reach higher-order modes we start seeing a drop-off of intensity within the central structure of the HG beam. The outside corner lobes maintain their intensity profiles while modes are increased to high orders, but at the same time the side lobes and central lobes lose their intensities (Figure 12(c)). This is not ideal for 3D structured

illumination in light-field microscopy. The reason being that the high intense corner lobes would generate additional photo-stimulation at those locations.

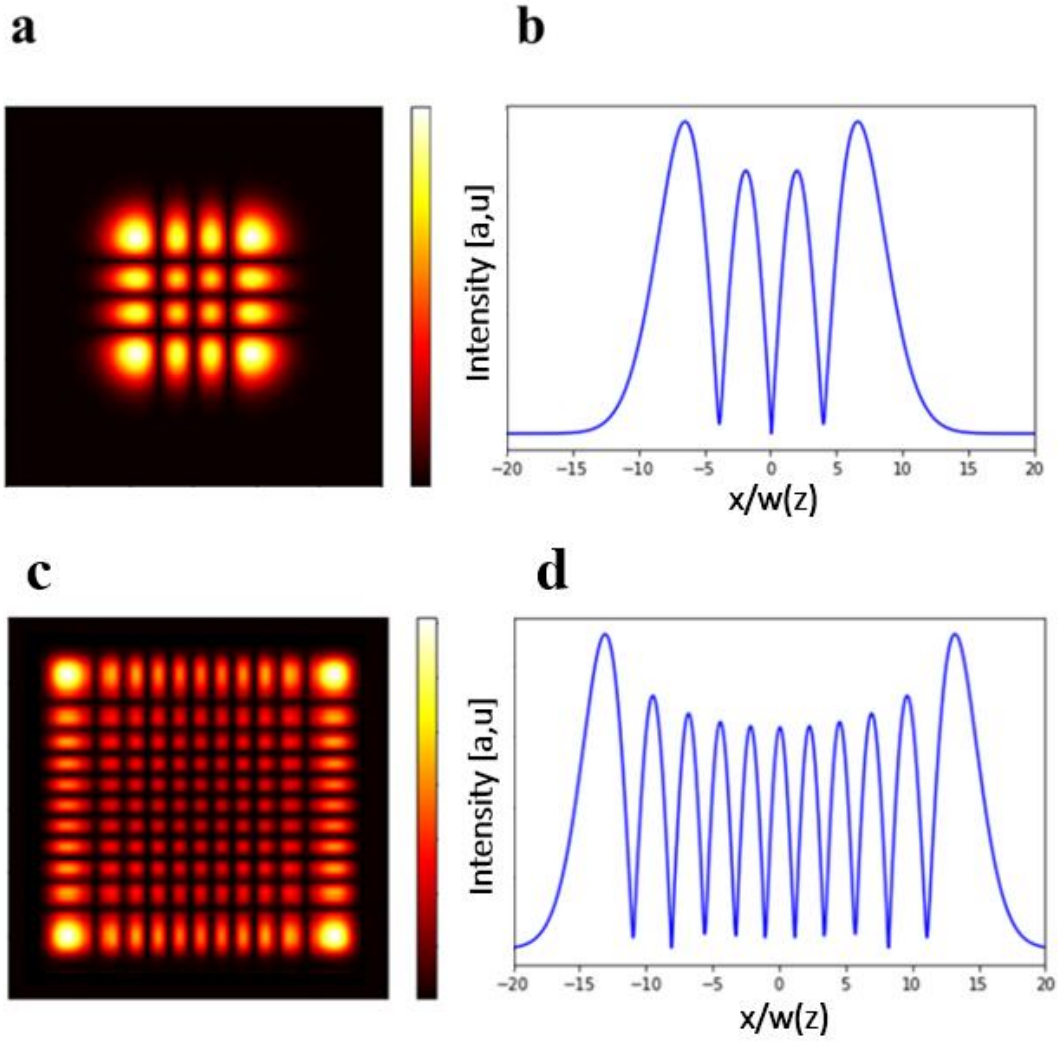

Figure 12: Low-order beam compared with a high-order beam to show the drop of intensity when going up to high-order. a) HG_{33} intensity profile b) 1D plot of a c) HG_{1010} intensity profile d) 1D plot of c

Modulated Hermite Gaussian Beams

In this section we will show how we approach a way to increase the intensity of the high-order HG beams by taking the envelope of the original HG beam in which we will invert and multiply it back to the original beam envelope to modulate the HG beam and have equal amplitude throughout the intensity profile. In this case I decided to use a super Gaussian function:

$$I(r,z) = I_p \, exp\,(-2\frac{r^3}{w(z)^3}) \qquad (7)$$

as my modulation function, which was similar to the inverted envelope of the original HG beam (Figure 13).

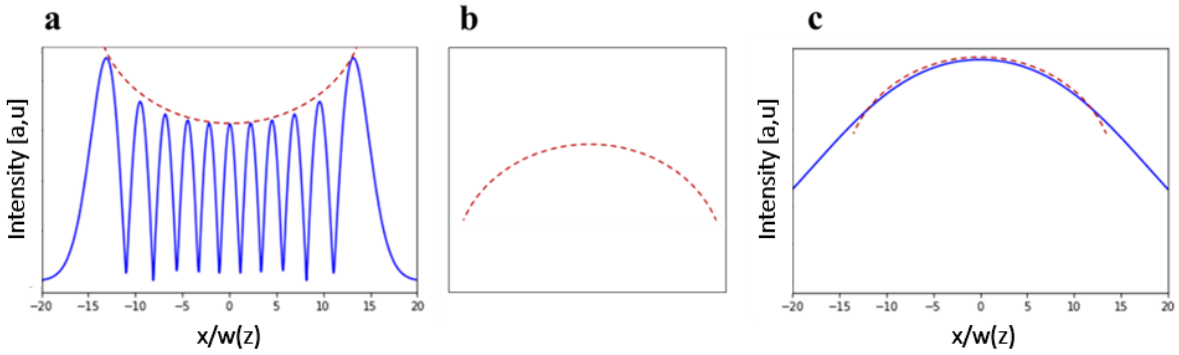

Figure 13: a) HG envelope b) Inverted HG envelope c) Comparison of inverted envelope to super Gaussian envelope

When the super-Gaussian envelope (Figure 13(c)) is multiplied by the original HG envelope (Figure 13(a)), we obtain the results that were expected. The intensity of the inner and side lobes is raised to that of the corner lobes (Figure 14(c)). This process can be applied to *nth*-

order modes, but you have to consider that the envelope of the original HG beam changes for *nth*-order modes. One must adjust the super-Gaussian envelope to that of the original HG beam. This can be achieved by adjusting the beam waist (w(z)) of the super-Gaussian function.

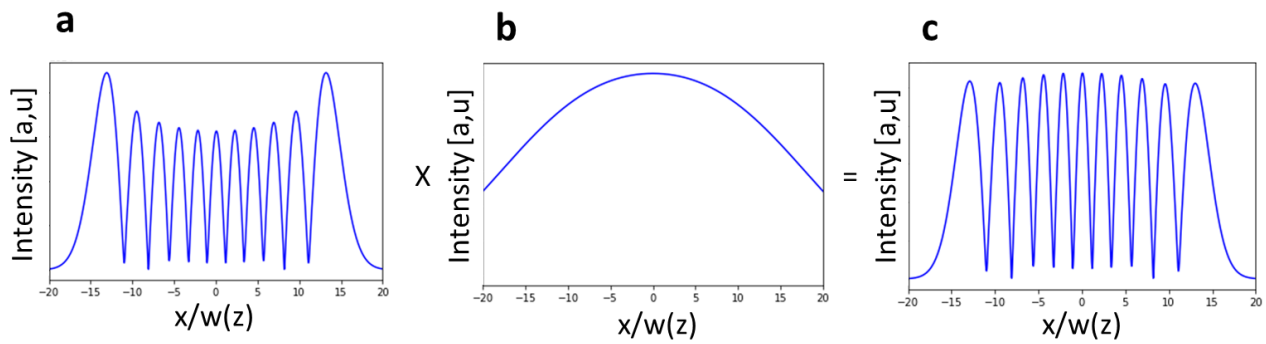

Figure 14: Process of modulating the original HG envelope to attain the modulated HG envelope. a) Original HG1010 envelope b) Super Gaussian envelope c) Modulated HG1010 envelope

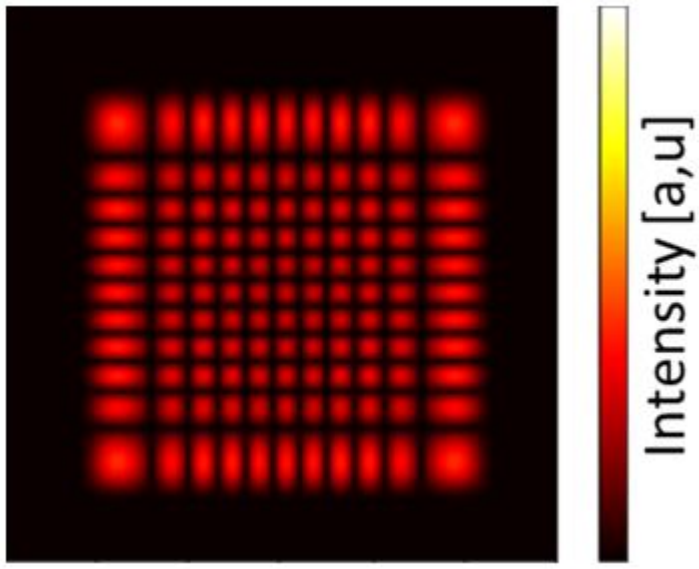

Figure 15: 2D Modulated HG1010 intensity profile

We have demonstrated that by modulating the original HG beam we were able to attain the modulated HG beam (Figure 15). Numerical results showed that the modulated HG beam has lobes of equal intensity. The next step would be to attempt to replicate these results experimentally and determine if the modulated HG beams will hold the non-diffracting and self-healing properties as the original HG beam. How these types of beams are created will be discussed in another section.

Spatial Light Modulator (SLM)

The Holoeye HES 6001 amplitude modulation-only Spatial Light Modulator (SLM) has a Liquid Crystal on Silicon chip (LCOS) with approximate dimensions of 15mm x 9mm. The Mai-Tai laser has a beam width of about 4mm and must be expanded. The beam is passed through 2 converging lenses, with focal lengths 12.5cm and 20.0 cm, resulting in a beam that is 1.6 times its original width. This allows the laser to take full advantage of the SLM. The SLM consists of a driver unit that accepts DVI or HDMI interfaces and a Liquid Crystal on Silicon chip (LCOS). It accepts a signal from a computer as an extended monitor device. The liquid crystal microdisplay is actually 1920 x 1080 pixel with each pixels being 8 μm. The electrical signal sent to the individual pixels changes the liquid crystal molecules such that their refractive index changes. Each of these changes affects the optical path length within that pixel. This allows for a phase change to be made to the wavefront of each femtosecond beam pulse.

HG Phase Masks

In order to experimentally create HG beams in the lab we have to produce an HG mask that can be displayed onto the spatial light modulator (SLM) in order to modulate the incident beam into an HG beam. Let's start with our HG(x,y) function which is stated to be the complex amplitude. We then applied a Fourier transform of the FT{HG(x,y)} and as a result we get the amplitude of the HG beam at z=0 in Fourier space. Then if we take an inverse Fourier transform of the amplitude, we get our resulting HG phase mask.

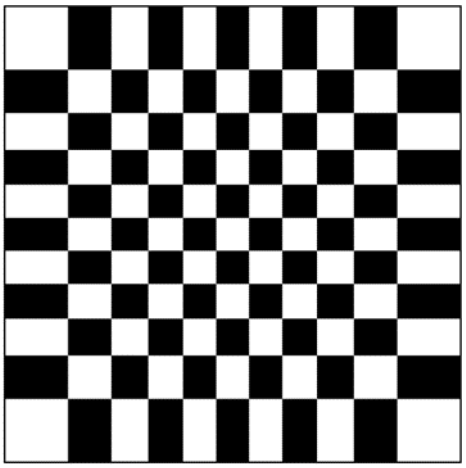

Figure 16: Example of the HG Mask. These are not the appropriate resolutions for use on the SLM. These are trimmed for presentation purposes. The appropriate phase masks must match the SLM resolution of 1920 x 1080 pixels and be centered for the SLM software.

This step is common for producing phase masks, but it's an important step to learn. HG masks are commonly used and there is nothing novel about creating them, but the importance of this process comes in handy once we modulate the original HG beam. The modulated HG masks are unknown and there are no references to show that you are on the right path. What we do

know is that if numerically we have produced a modulated HG beam, we can respectfully take the inverse Fourier transform of such beam and get the resulting mask from it. The only way to determine the continuity is by displaying the resulting modulated HG phase masks onto the SLM.

Truncated HG Phase Mask

Another approach taken to control the modulation of high-order Hermite Gaussian modes was done by manipulating the phase of the original HG phase mask. This method was introduced by Hemant Kumar Meena and Brijesh Kumar Singh from the Central University of Rajasthan. In their method an annular binary phase mask was introduced. The phase mask consisted of two sections with opposite phases given by

$$P(r) \propto \begin{cases} -1 & r \leq r_\pi \\ 1 & r_\pi \leq r \leq r_{max}, \end{cases} \tag{8}$$

where $0 < r_\pi < r_{max}$, $r_\pi = \gamma\, r_{max}$, $r_{max} = d/2$, d is the diameter of the mask aperture, and r is the radial coordinate. r_π is the π phase-shifted radial length, where γ is the coefficient that varies from zero to one ($0 \leq \gamma \leq 1$). By changing the numerical value of γ , one can vary the π phase-shifted radial length r_π which plays a factor in the modulation of the HG beam. By increasing or decreasing the internal binary sector in contrast to the external binary sector of the mask, the intensity of the HG beam can be modulated (Meena & Singh, 2022).

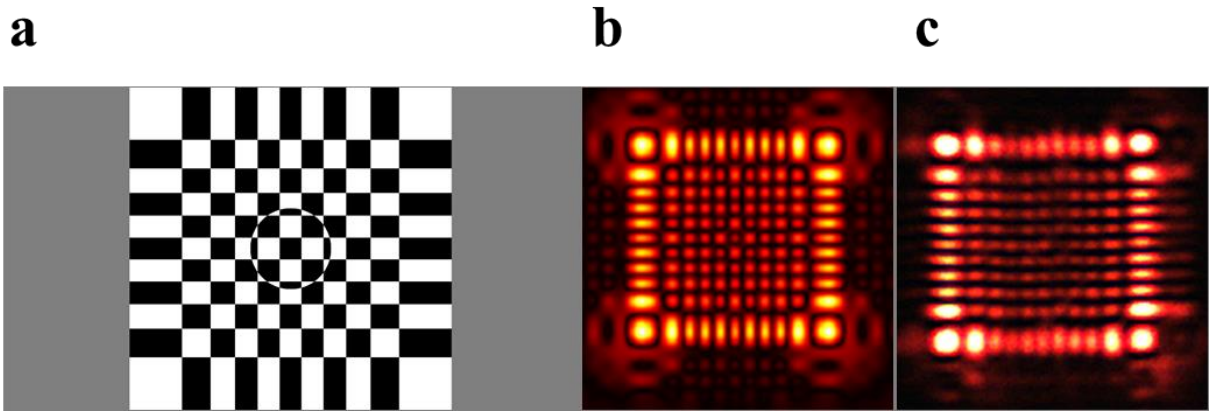

Figure 17: a) Annular binary phase mask b) The theoretical Fourier transformed 2D intensity profile of a c) The experimental Fourier transformed 2D intensity profile

These HG masks were reproduced in the lab and tested experimentally. As a result, we found that the equal amplitude modulation of the higher-order HG beams couldn't be achieved with their method (figure 17).

The idea of using a truncated HG beam phase masks originated from using their method of the annular binary phase mask and changing the parameter as

$$P(r) \propto \begin{cases} 0 & r \leq r_{\pi} \\ 1 & r_{\pi} \leq r \leq r_{max}, \end{cases} \tag{9}$$

where changing the value to 0 truncates the internal phase instead of inverting the phase as was proposed. The idea of truncating the phase information that produces the high intense corner lobes and side lobes came from knowing that HG beams hold their self-similar property. If the phase only holds the information to produce a truncated HG beam, then the Fourier transform of the mask will produce truncated HG beams. As shown in (figure 18) the theoretical approach

shows that this theory followed. The numerical results showed the modulation of the HG beam had equal amplitude by truncating the outer lobes and only keeping the inner lobes. The next step would be to see if the beams can now be produced experimentally, and the most important part is if they hold their non-diffracting properties.

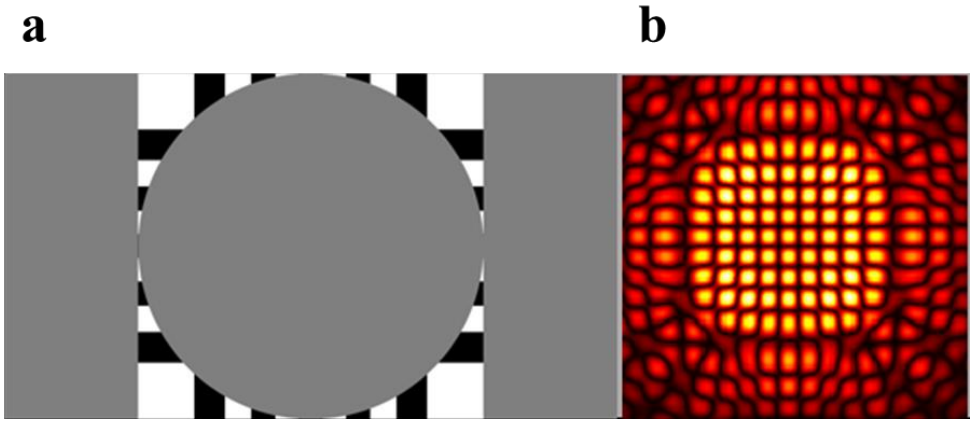

Figure 18: a) Truncated HG beam phase mask b) The theoretical Fourier transformed 2D intensity profile of a

Optical Fourier Transform

When the incident laser sends a pulse to the SLM, the SLM changes the phase front of the pulse. The phase front has the inverse Fourier transform of the HG function encoded in the transverse direction. The modulated beam passes through a lens, the lens performs a Fourier transform on the modulated beam. One obtains a so-called Fourier plane at a distance of one focal length after a thin lens (Figure 19). This process mirrors the process we applied to the making of the HG masks. If we know what beam we would like to produce after the Fourier lens,

we must first produce the inverse Fourier transform of it. In the example of the modulated HG beam, we know that numerically it can be produced. Now by taking the inverse Fourier transform and encoding it on the SLM, the modulated HG beam should be produced after the Fourier lens.

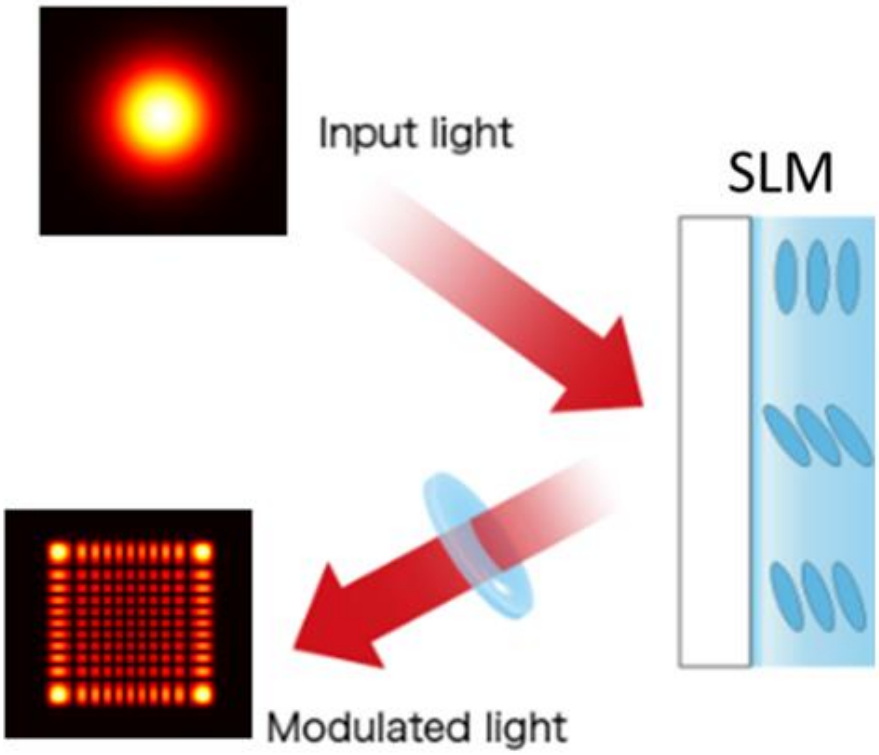

Figure 19: Optical Fourier Transform

Spatial Filtering

An issue that we have encountered with the Holoeye HES 6001 SLM is an additional reflected 0^{th} order beam. The 0^{th} order light is focused on the same plane as the modulated beam (1^{st} order) and can be seen in the center of the image plane (Figure 20). A way to remove this unwanted 0^{th} order is through the process of spatial filtering. A spatial filter is an optical device that uses the principles of Fourier optics to alter the structure of a beam. Spatial filters are commonly used to block 0^{th} order light at the focal plane. The focal plane is also referred to as the Fourier plane. However, since both the 0^{th} order and 1^{st} order light come into focus at the same plane, a diffraction grating is superposed on the phase profile of the HG phase mask. The diffraction grating will axially shift the 1^{st} order from the 0^{th} order, making it possible to filter out the 0^{th} order and let the 1^{st} order through. In our case the $\pm 1^{st}$ order diffracted beams are HG beams.

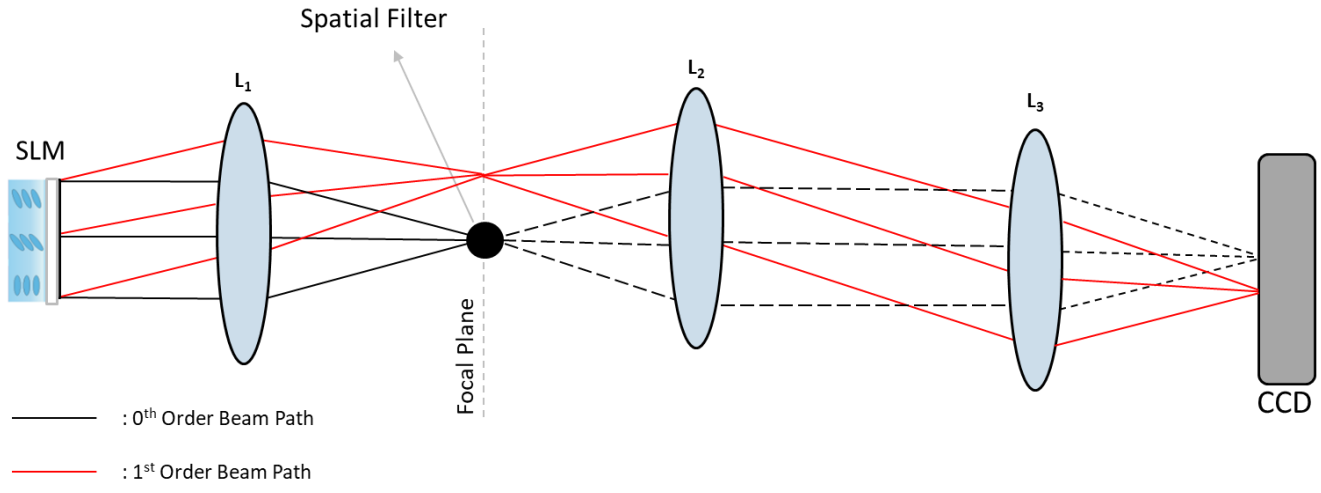

Figure 20: Optical setup showing placement of spatial filter at the focal plane

Light-Field Microscope Setup

The proposed 3D structured illumination light-field microscope is shown in Figure 17. The laser beam is expanded with a telescope to match the active region of the SLM. After the SLM, only the 1st order beam will be picked through a spatial filter. This HG beam goes through an illumination lens and objective lens, where then the beam illuminates on to sample. The fluorescence signal will be epi-collected through the same objective lens, to infinity-corrected tube lens to focus the image from the infinity-corrected objective, and the MLA to form a light-field image. Ideally the camera sensor is placed at the back focal plane of the MLA. However, the focal length of MLA is very short, about a few millimeters. Therefore, a relay lens (RL) is attached to the camera which can project the back focal plane of MLA onto the camera sensor plane. In Objective 2 another lens (OL 2) will be placed in the orthogonal direction of the 7 original objective lenses (OL 1), and the fluorescence signal is still collected through OL 1. The HG beam will be scanned in space to illuminate all volumes within the sample.

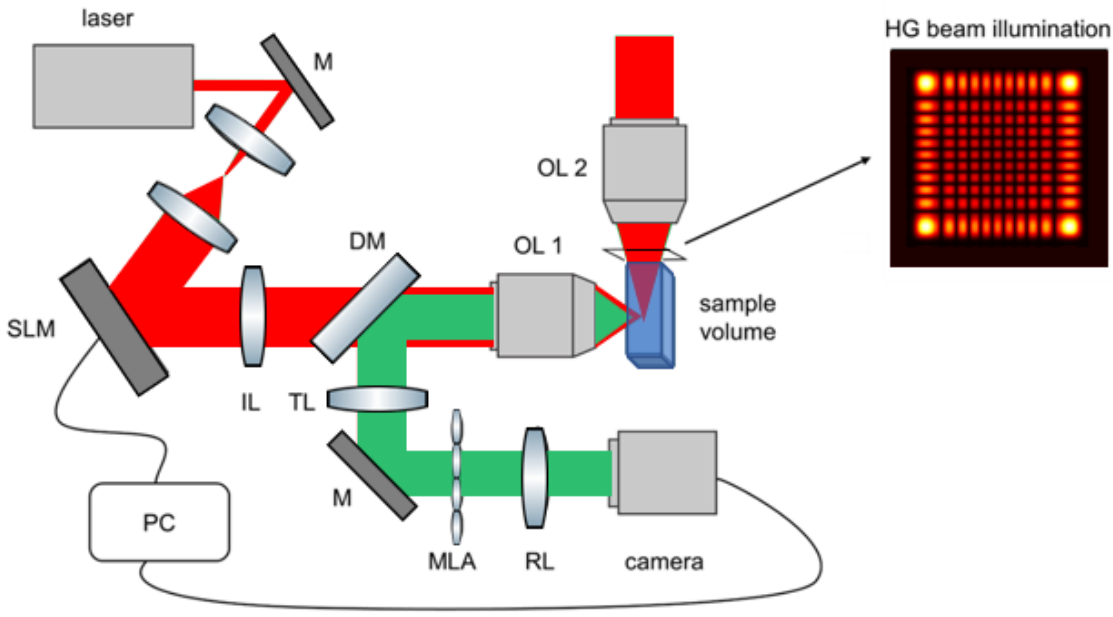

Figure 21: Light-field microscope setup with HG beam structured illumination

Results

There were two approaches taken to modulate the original HG beam. One approach was through modulating the envelope of the HG beam and the other approach was through truncating the HG phase mask. Each of these phase masks was displayed on the SLM to compare the numerical approach and the experimental results. As shown in Figure(22), the numerical results are identical to the experimental results.

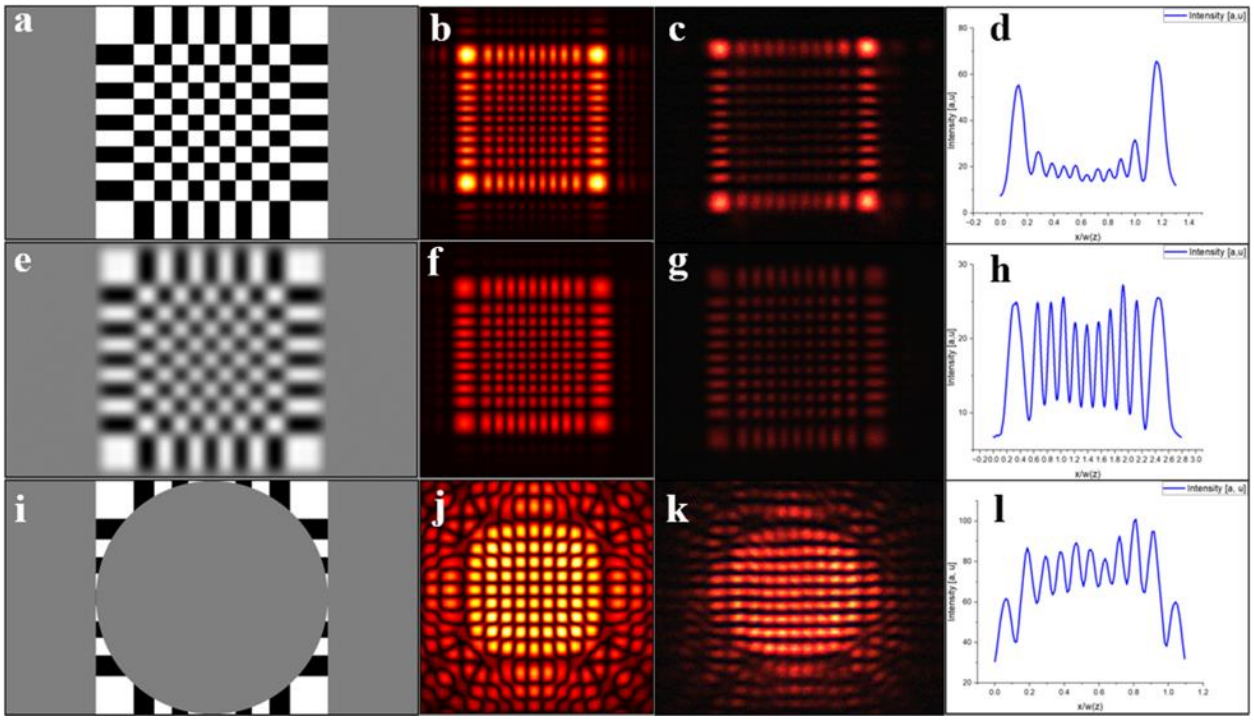

Figure 22: The first row shows the original HG_{1010} mode while the second row shows the modulated HG_{1010} mode, and the third row shows the truncated HG_{1010} mode. First column (a, e, i) corresponds to the phase masks, second column (b, f, j) corresponds to the theoretical Fourier transformed 2D intensity profile of the first column, third column (c, g, k) shows the experimental Fourier transformed 2D intensity profile, and fourth column shows the intensity plot profile of the third column.

We were able to show from the results that the modulation of the original HG beam was achieved. The modulated HG_{1010} mode showed the best results as it retained the shape of the original HG beam. The intensity distribution of the corner and side lobes was reduced while the lobes within the center of the HG beam were increased. As for the truncated HG_{1010} mode, the corner and side lobes were truncated and only retaining the central lobes. The central lobes show higher intensities than compared to the original and modulated HG beams, but it lacks the structure of the original HG beam due to the constructive and destructive interference patterns. Both of these approaches show promising results in modulating the intensity profile of the HG

beam. The next step was to see if the modulated and truncated beam would hold the non-diffracting properties of the original HG beam. In order to determine the non-diffracting properties, each beam was characterized by taking images of the beam through a change in z (Δz). This determines how the beam propagates in z and for how long it holds its profile before diffracting.

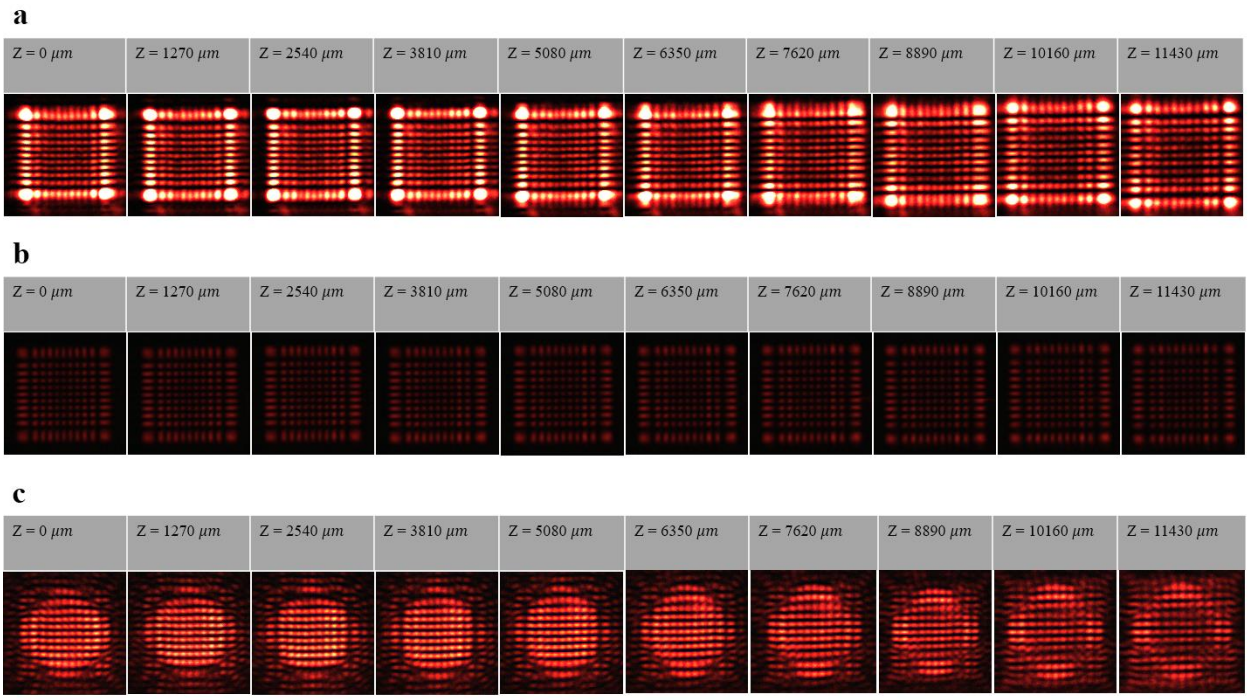

Figure 23: a) Original HG beam propagation b) Modulated HG beam propagation c) Truncated HG beam propagation

From figure (23), we can see how each beam propagates as it moves through space. As expected, the original HG beam holds its non-diffracting properties while it travels through ~10mm (10,000μm) in z. If you compare the beam at z=0 and z=11,430 μm the profile of the beam is unchanged. The modulated beam's propagation seems promising compared to the original HG beam propagation. As the modulated beam travels through ~10mm in z, its profile

holds its shape with a few shifts in the central structure, but if you compare the beam at z=0 to z=x the structures are similar. Then what could be said is that the modulated HG beam holds similar non-diffracting properties to that of the original HG beam.

When propagating the truncated HG beam through ∼10mm in z, at ∼1mm in z the beam begins to diffract. It does not hold its intensity profile through propagation. The reason why could come from losing the corner and side lobes. The corner and side lobes play an important part in the self-healing process of the HG beam. Evidently, the power of the beam flows from the side lobes toward the corner lobes to facilitate self-healing. The self-healing of the beam provides the beam to be non-diffracting as it propagates. While truncating the corner and side lobes, the internal transverse power flow is disrupted, and the self-healing properties vanish. As for the modulated HG beam, the corner and side lobes are present, and the transverse power flow is not disrupted holding on to the self-healing properties.

Conclusions

In this work we have demonstrated both theoretically and experimentally the process of modulating the intensity profile of optical HG beams. Experimentally we also showed the self-healing properties of both unmodulated and modulated HG beams by propagating them through space. We have demonstrated that by losing the corner and side lobes of the beam the self-healing property vanishes and the non-diffracting property is lost when propagated. We believe that the robust nature of the modulated HG beam can be implemented into the LFM to achieve deeper penetration and overcome tissue scattering in biological tissues.

Chapter 2: Two Photon Fluorescence Imaging of Nanoscale Sulfur

Two-Photon

Two-photon absorption (TPA) is a nonlinear optical process in which the absorption coefficient depends on the optical intensity. In the process of two-photon absorption, an atom makes a transition from its ground state to an excited state by the simultaneous (< 1 fs) absorption of two photons. This was first theorized in 1931 by Maria Goeppert Mayer in her dissertation. It would take 30 years before she was proven to be correct by Kaiser and Garret in 1961(Paez, 2019).

In the case of the conventional (one-photon) excitation, an electron can absorb energy from impinging photons of some energy, where the energy E of the photon is given as

$$E_{photon} = \frac{hc}{\lambda_p} = h\nu \tag{10}$$

where h is Planck's constant, c is the speed of light, λ_p is the wavelength of the single photon, and ν is the photon frequency, and subsequently emits photons of some energy less than the original photon energy. Assuming that the system's electron is in the ground state S_0, the electron will absorb the incoming excitation photon, with energy E_{excite}, giving the system some energy $h\nu$. The electron is excited to the next excited state S_n. The amount of time the electron stays in the excited state is called the relaxation time and is on the order of nanoseconds. When the

electron falls back down to the lowest excited state, it will emit a photon of energy $E_{fluorescense}$. The emitted photon must have a longer wavelength than the excitation photon that was absorbed.

$$E_{excite} > E_{fluorescense} \tag{11}$$

$$\frac{1}{\lambda_{excite}} > \frac{1}{\lambda_{fluorescense}} \tag{12}$$

$$\lambda_{fluorescense} > \lambda_{excite} \tag{13}$$

In TPA, the excitation is produced by two lower energy photons of identical or different frequencies that arrive nearly simultaneously, within a femtosecond (10^{-15} of a second), to sum together.

$$E_{excite} = \frac{hc}{\lambda_1} + \frac{hc}{\lambda_2} = \frac{hc}{2\lambda_p} \tag{14}$$

In the case of our two-photon microscope via a pulsed femtosecond laser. The two photons will carry the same energy, and the absorbed energy will be twice the photon's energy $2E_{2p}$. The process follows with the electron dropping down to the ground state and emitting a photon. The only significant difference is that the fluoresced photon energy will be less than the sum of the energies of the excitation photons,

$$\lambda_{fluorescense} < 2\,\lambda_P \tag{15}$$

where it can be stated that two-photon fluorescence is said to occur when two photons are absorbed simultaneously, and one photon emitted is of less energy than the 2 excitation photons summed. Therefore, systems with visible one-photon excitation transitions can be excited with

infrared (IR) and near-infrared (NIR) wavelengths that range from 680nm-1040nm. The Jablonski energy diagrams for one-photon and two-photon excitations are shown in (Figure 24).

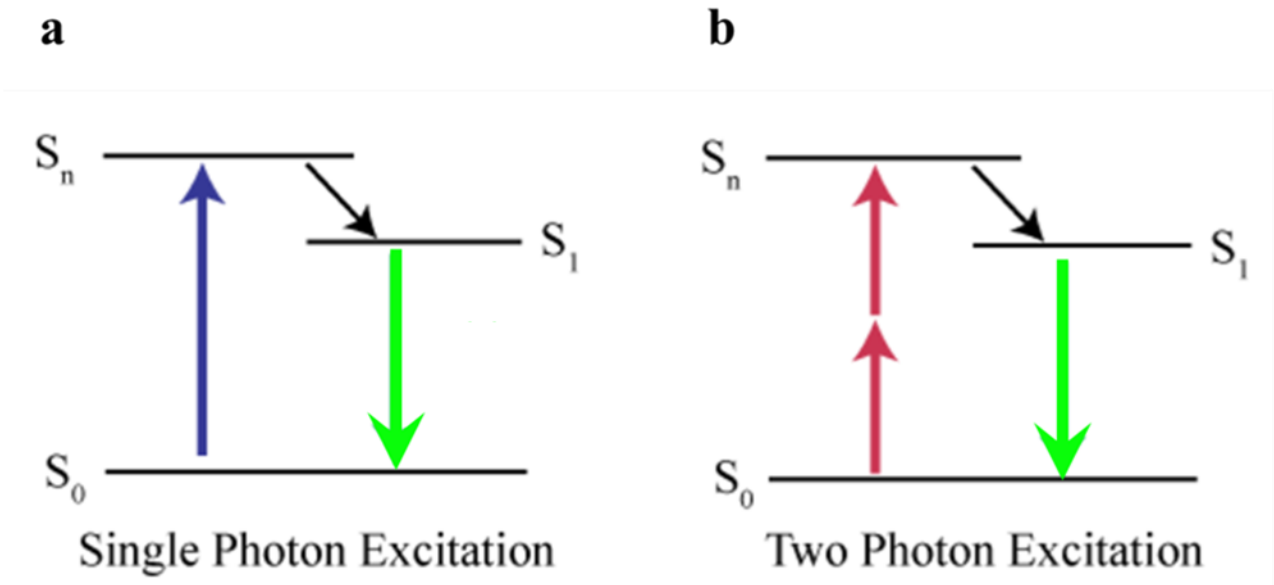

Figure 24: Jablonski energy diagrams for a) single-photon and b) two-photon excitation.

The probability of two-photon absorption occurring is dependent on the square of the intensity of the impinging light, which is expressed as,

$$P_{2PA} \propto \sigma I^2 \tag{16}$$

where P_{2PA} is the probability, I is the intensity of the light impinging on the material, and σ is the unit of the two-photon molecular cross section that quantifies a molecule's propensity for two-photon absorption. The unit is defined as 10^{-50} cm^4 s (photon molecule)$^{-1}$. In order to increase the probability of TPA, a second photon has to be absorbed during the short lifetime within a femtosecond of the virtual state. The high intensities of light required for two-photon absorption

can be achieved through photon confinement. Spatial and temporal photon confinement methods are combined to help concentrate the photon density high enough to cross the threshold for non-linear optical processes. Spatial confinement happens when the photons traveling through some cross-sectional areas are converged to a very small spatial volume, increasing the photon density at the point of focus. Temporal confinement happens when the photons produced in time are compressed into smaller packets. By utilizing ultrashort pulsed lasers to ensure the photons arrive at the same time.

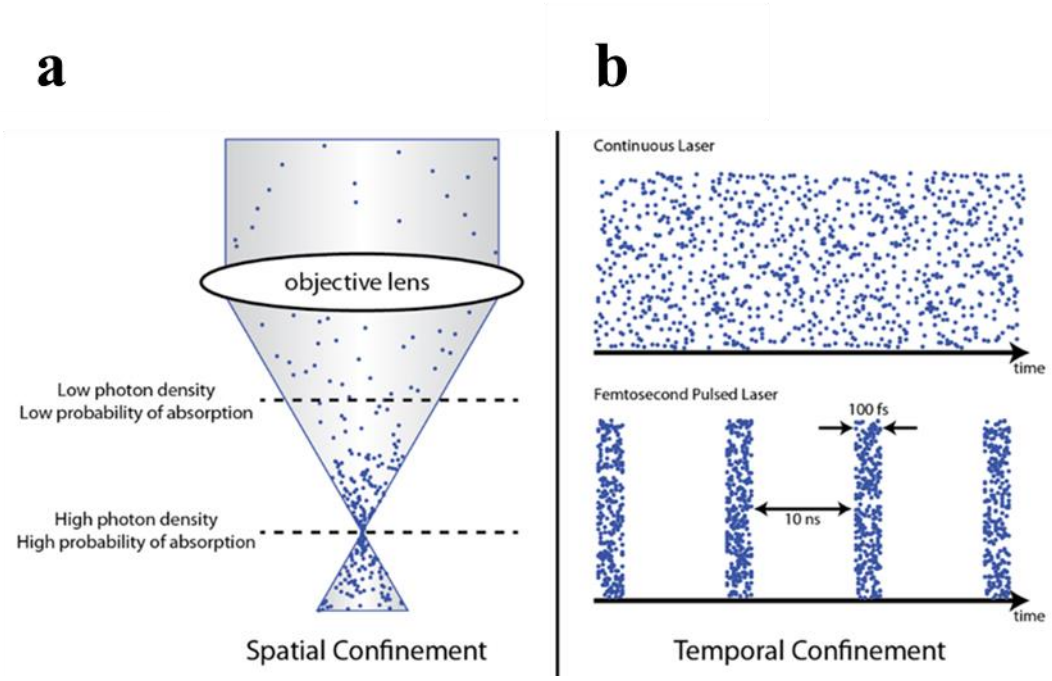

Figure 25: Photon confinement a) Spatial confinement b) Temporal Confinement. Image from Durst biomedical optics research group et al. (2022)

Advantages of Two-Photon Microscopy

The advantage that arises due to the quadratic dependence of TPA on the intensity, the probability of TPA at the point of focus is much greater than that of the outside of the focus. Thus, the TPA occurs only at the center of the focus where the photons are confined both spatially and temporally. As for the case of one-photon absorption, it depends linearly on the excitation intensity. As the light focuses, everything within the single photon focus plane will undergo excitation. This is inconvenient due to the extra fluorescence that can cause photobleaching of the signal and also photodamage to the tissue that's being visualized throughout the entirety of the sample.

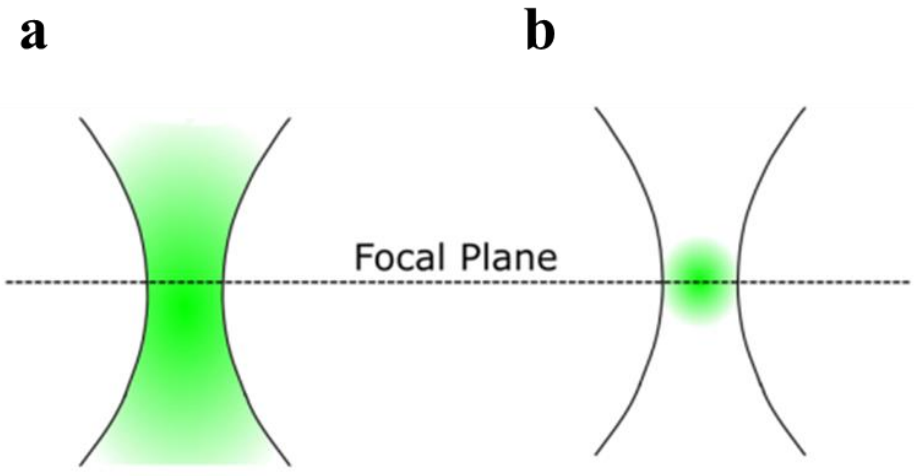

Figure 26: a) Single-Photon b) Two-Photon

Imaging depth is also another advantage that two-photon microscopy has over the conventional microscope. The property of light scattering is one of the main factors that control how deep one can image through thick tissue samples. Due to the fact that the excitation light

used in two-photon microscopy is infrared, there will be less light scattering than excitation light in the visible spectrum (Benninger & Piston, 2013b).

Two-Photon Microscope

To attain the higher photon density required to cross the threshold for non-linear optical processes, a pulsed laser is used in combination with a high numerical aperture objective lens. The laser used in the biophotonics lab is a femtosecond pulsed Ti: Sapphire tunable laser source (Spectra-Physics, Mai Tai SP). Its pulse duration is about 100 fs with a repetition of 80 MHz. The wavelength of the laser is tunable from 690 nm to 1040 nm, with a maximum power up to 2.5 W. A combination of a half-wave plate (HWP) and polarizing beam splitting (PBS) cube is used to adjust the amount of power delivered at the sample location. The HWP is rotated to rotate the polarization of the beam and the PBS cube is used to transmit vertically polarized light. The laser is raster scanned in the x-y plane. A polygonal mirror with 36 faceted mirrors that spins at 480 revolutions per second, scans in the horizontal x-direction and a Galvano mirror scans the beam in the vertical y-direction to produce a 2D light sheet. With the current setup, we are able to collect a two-dimensional image (350um x 350um) at a rate of 30 frames per second. The objective lens focuses the light sheet onto the sample where then the epifluorescence of the sample is collected by the same objective lens and passes through a series of dichroic mirrors and bandpass filters to the photomultiplier tubes (PMTs) where the photons are converted into electrical signals. Dichroic mirrors are used to transmit a certain wavelength while reflecting another wavelength. The Epi-fluorescence signal is split into its red, green, and blue (RGB)

components by the dichroic mirrors and filtered by bandpass filters of 417−477 nm, 500−550 nm, and 570−616 nm, into their respective photomultiplier tubes as shown in (Figure 27). The samples are mounted on a three-dimensional motorized stage (Shutter Instrument, model MP-285) which allows us to record images and videos at a given xyz-position.

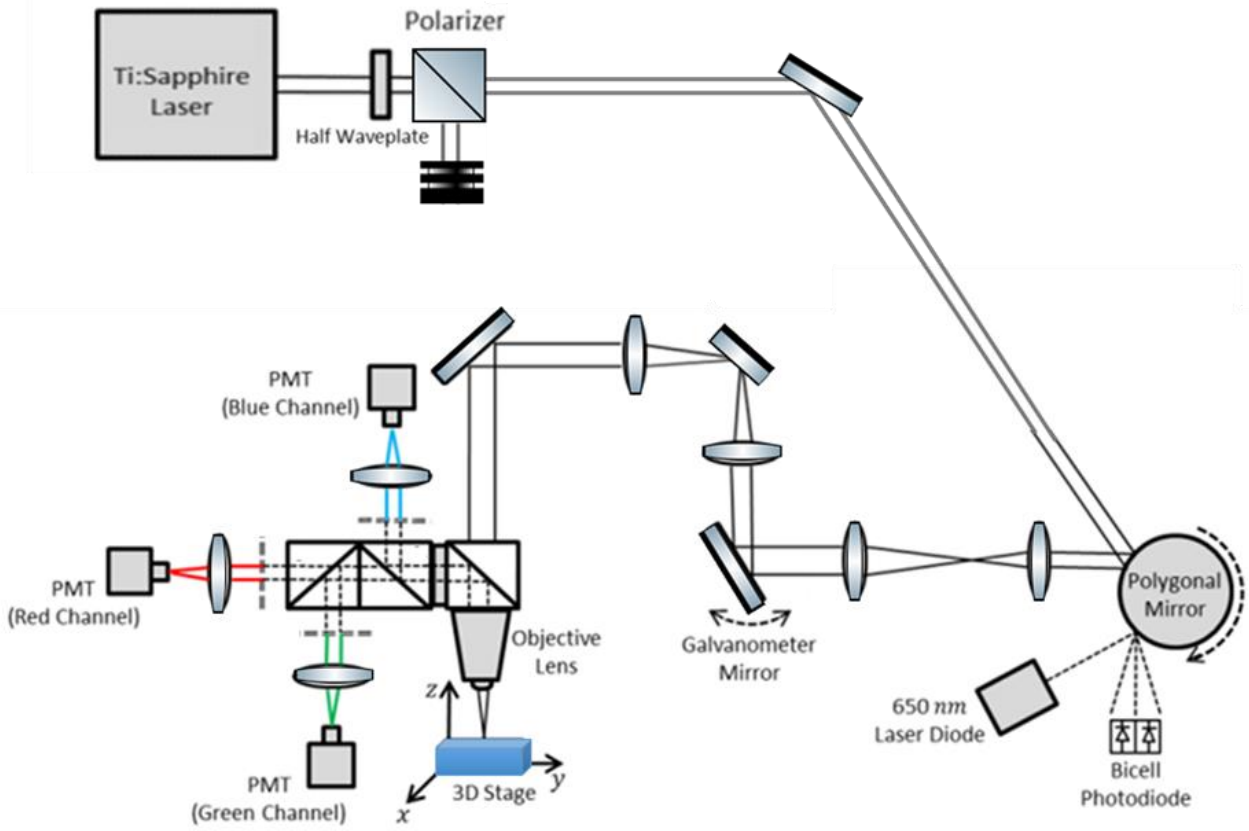

Figure 27: Schematic of the Two-Photon Laser Scanning Fluorescence Microscope developed in the Biophotonics Laboratory of the Physics Department at UTEP.

Nanoscale Sulfur to Suppress Disease in Tomatoes

By the year 2050 the global population is estimated to have reached 9 billion. In order to keep up with the food supply, agriculture production will have to increase by approximately 70% by 2050. One of the factors stepping in the way of increasing production is the infectious diseases in plants. Pathogens reduce crop yields by up to 20% and compromise product quality, often leading a 40% loss before harvest (Wang et al., 2022). Recent work has shown the potential of nanoscale micronutrients to enhance tolerance to biotic and abiotic stressors. In this case, nanoscale sulfur can be used to enhance crop nutrition and suppress disease. Pristine (nS) and stearic acid coated (cS) sulfur nanoparticles were added to soil planted with tomatoes at 200 mg/L soil and infested with Fusarium oxysporum.

Two-Photon imaging of Nanoscale Sulfur

Two-photon microscopy was used to detect the root uptake and determine the biodistribution of nanoscale sulfur with an average particle size of ~65 and ~38 nm. Characterization of pristine, stearic acid coated, and bulk sulfur was done to determine their fluorescent signal properties. The Single-photon excitation wavelength of nano sulfur ranged from 320 to 460 nm and emitted fluorescence within the range of 424 to 542 nm. This follows what we know about single-photon absorption $\lambda_{fluorescense} > \lambda_{excite}$. With this information, I was able to run a wavelength scan on the nano-sulfur using our two-photon microscope. The wavelength scan ranged from 690 to 1040 nm. For the first attempted wavelength scan, nano

sulfur was detected within the 710 to 810 nm wavelength range but achieved the best two-photon fluorescent signal at 720nm at a power intensity of 150mW.

Figure 28: Pristine nano sulfur fluorescent signal before sonification

As you can see from (Figure 28), the fluorescent signal from the nano sulfur was detected by two-photon absorption, but for the amount of sample that was prepared onto the glass slide, little to no detection was made under the light sheet. This led my collaborator and I to realize that nano sulfur is size dependent. New nano-sulfur particles were prepared by my collaborator. The sulfur was ground to a finer powder to ensure dispersion within the particles and then suspended

in DI water (500 mg/L). The sample was then sonicated to reduce particle aggregation and the formation of clusters. After sonication, the sample was placed back into the two-photon microscope and the signals from the nano sulfur were evident as shown in (Figure 29).

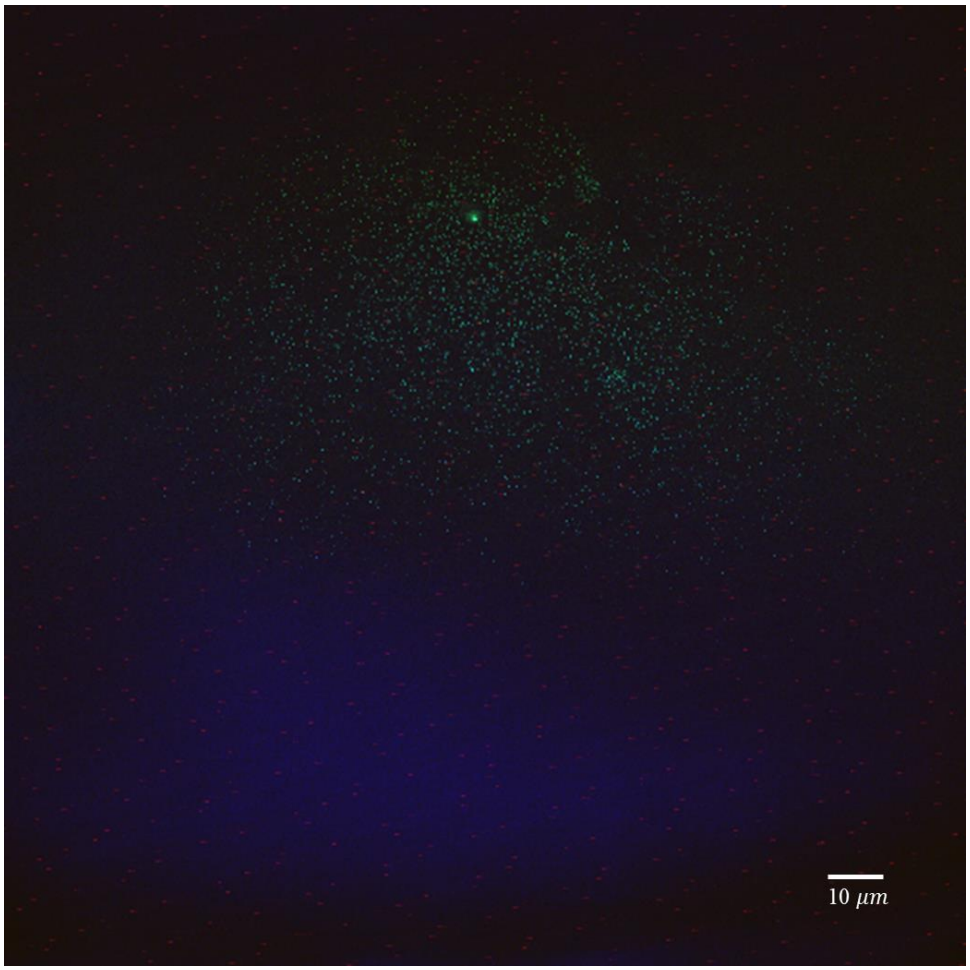

Figure 29: Pristine nano sulfur fluorescent signal after sonification

The same characterization methods were used to detect bulk sulfur and stearic acid-coated nano sulfur particles. Neither bulk sulfur with or without sonication nor steric acid-coated nanoscale

sulfur exhibited detectable fluorescence. Steric acid-coated nanoscale S did not fluoresce, likely due to the altered surface chemistry.

In Vivo Root Uptake of Nanoscale Sulfur

The in vivo root uptake of nanoscale sulfur and translocation of the particles to the leaves or other tissues throughout the plant were tracked through two-photon microscopy. This method was used to prove that the nano sulfur was up taken from the soil sample and determine where the plant was storing the particles. Previously the two-photon excitation of nano sulfur was determined to have the best distinguishable fluorescence signal at 720nm. Taking this parameter into account, control samples of tomatoes' roots and leaves were looked at under our two-photon microscope at 720nm at 150mW. Analyzing the control samples, autofluorescence signals were detected from both root and leaf samples. Autofluorescence in plant tissue is a common phenomenon arising from a variety of biomolecules that absorb light. In this case a very useful phenomenon for in vivo imaging of the root uptake of nano sulfur.

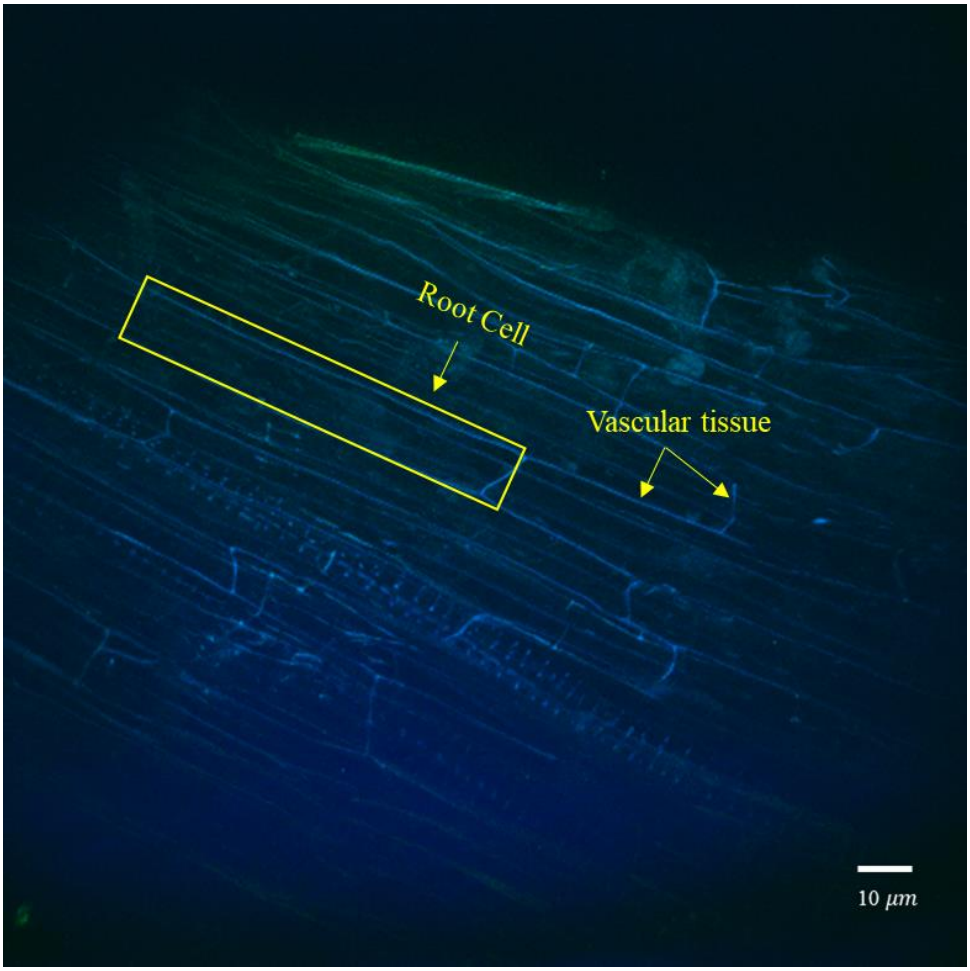

Figure 30: Autofluorescence signal from control root sample

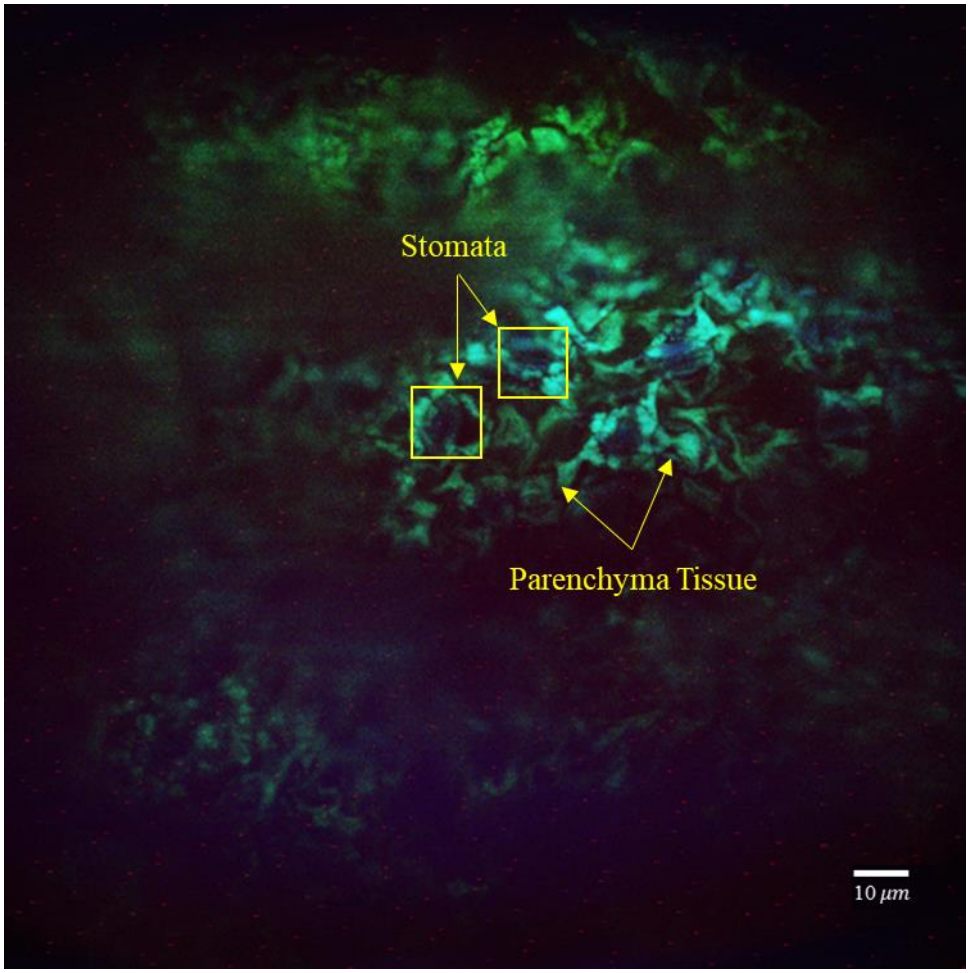

Figure 31: Autofluorescence signal from control leaf sample

The characterization of the nano-sulfur particles and control plant samples can now be used as a reference to compare with the treated tomato samples. The first sample that was imaged under the two-photon microscope was the sample grown under 200 mg/L pristine nano-sulfur treated soil. Both pristine nano sulfur and the plant samples fluoresced at 720nm and the background autofluorescence did not interfere with the sulfur signals. Detection of pristine nano sulfur was detected along the vascular tissue and cells of the root samples. Multiple images were taken along the root to determine the uptake process and to ensure that the translocation to the

leaf samples was accurate. A technique termed “z-scan” was applied during the imaging process to acquire a 3D volumetric image of the root sample. The z-scan process consists of taking a light sheet and exciting a plane in the x-y direction at a single z location, usually at the top surface of the sample. After taking the top surface image you move the light sheet only in the z direction towards the sample and gather an image at the next Δz location. In our case, a $\Delta z = 10\mu m$ step size was used to acquire $400\mu m^3$ volumetric image which added up to 40 images to reconstruct and acquire that 3D image. The information that was gathered from the reconstructed 3D image, was to determine if the nano sulfur was truly within the root sample and not on just the surface. The results showed that the sulfur was within the root cells and now we could move on to the leaf samples.

The autofluorescence signal was more intense in the tomatoes’ leaf sample but did not interfere with the detection of the pristine nano-sulfur. The majority of the nanoparticles were localized in the tiny pores present on the plant tissue of the leaves known as the stomata. One of the functions of the stomata is to release excessive water through the form of water vapor. So, it could in fact explain why the translocation of the pristine nano sulfur ended up at the stomata. From tracking the pristine nanoparticle from the root to the leaf, we could conclude that the uptake of the nanoparticles was achieved.

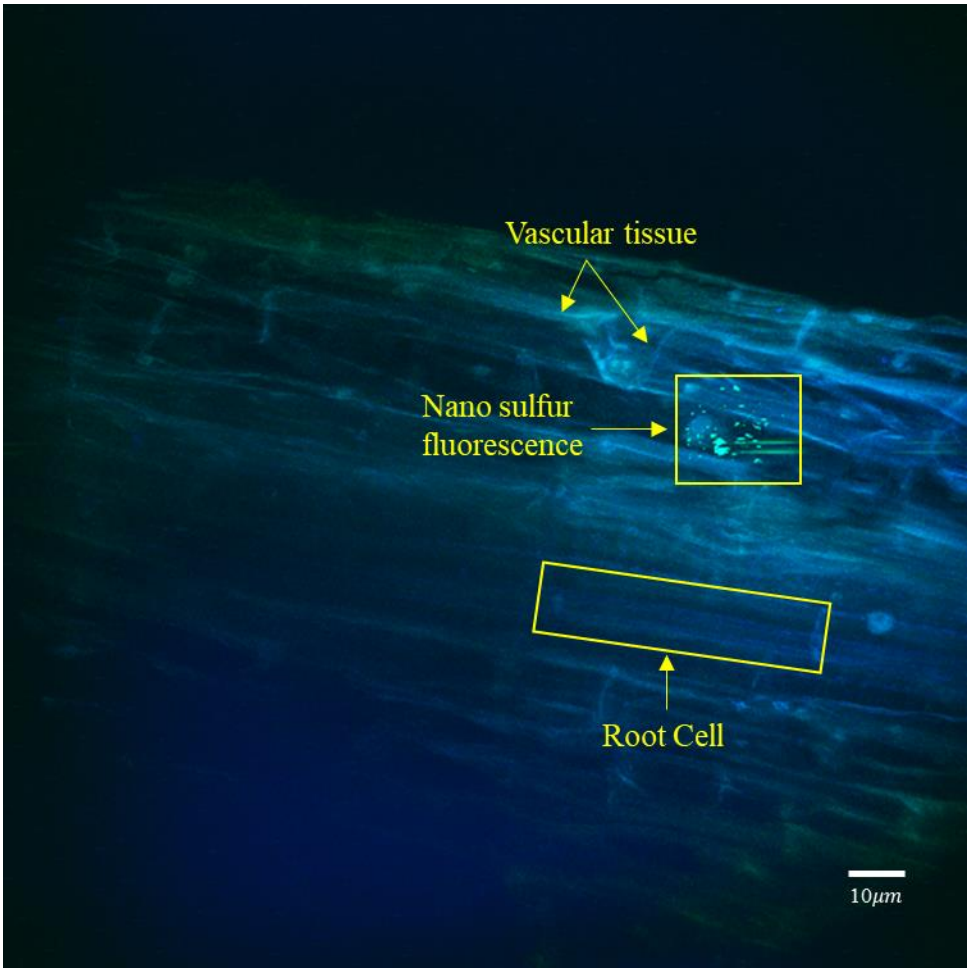

Figure 32: Pristine nano sulfur fluorescent signal found within root sample

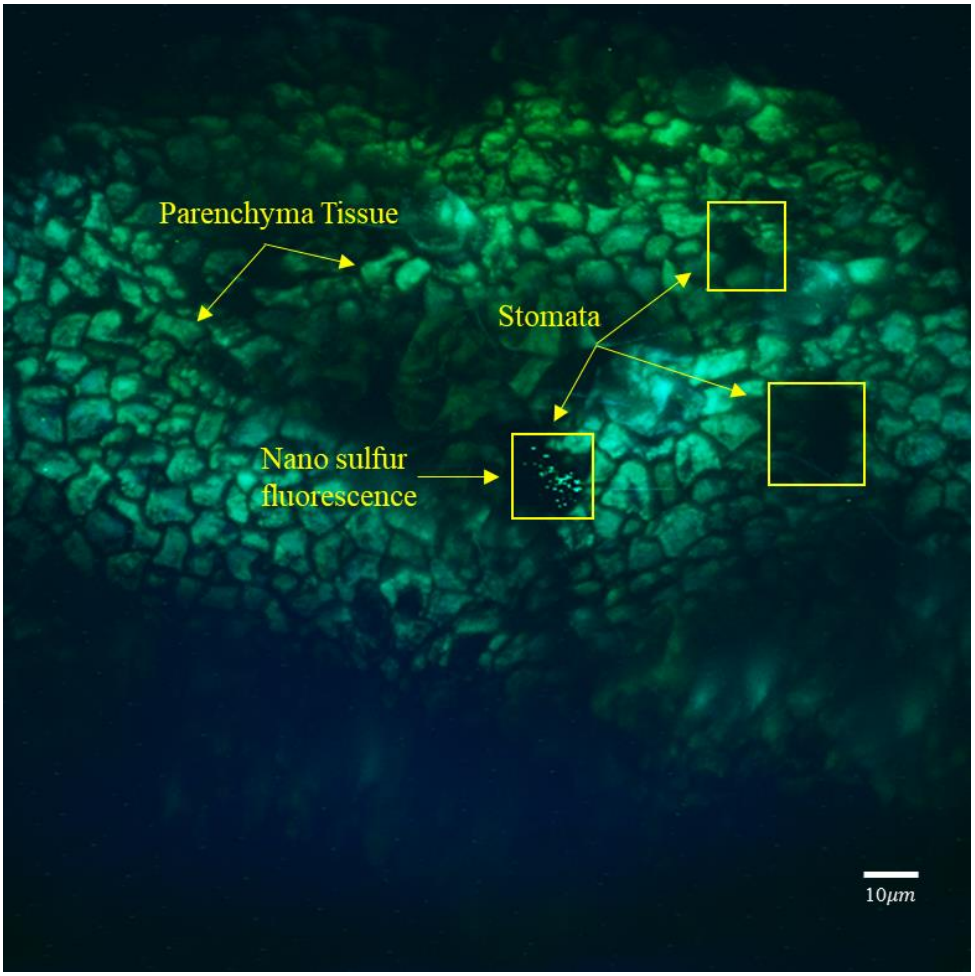

Figure 33: Pristine nano sulfur fluorescent signal found within leaf sample

The second sample imaged was grown under 200 mg/L of bulk sulfur-treated soil. In previous experiments, it was determined that bulk sulfur didn't fluoresce under the two-photon microscope. When looking at the samples treated with the bulk sulfur, surprisingly we saw fluorescent signals similar to those that we saw with the samples treated with the pristine nano sulfur particles. Considering that the fluorescence of sulfur is size dependent, our guess is that during the uptake process the bulk sulfur was broken down to nano size. Following the same procedures as before, it was determined that there were fluorescent sulfur particles within the

root cell and translocated in the stomata as shown in the previous sample. As for the stearic-acid coated sulfur nanoparticles, there was no fluorescent signal detected. This followed when imaging the plant samples that were grown in 200 mg/L stearic acid-coated sulfur nanoparticles treated soil. There was no detection of any nanoparticle signal within the samples.

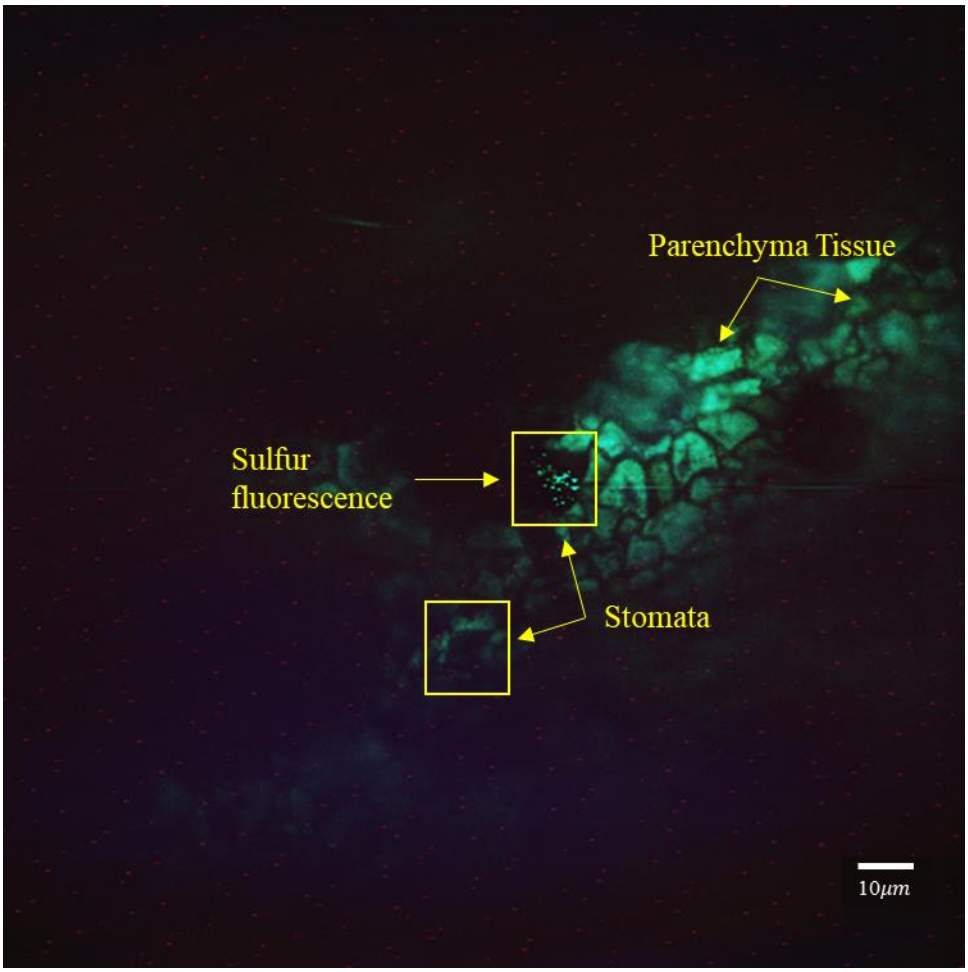

Figure 34: Sulfur fluorescent signal found within leaf sample from bulk sulfur soil sample

Conclusion

After the characterization of pristine nano sulfur, stearic acid-coated nano sulfur and bulk sulfur, we have concluded that the fluorescent signal was size and coating dependent. By ensuring particle aggregation and the formation of clusters within the pristine nano sulfur sample we were able to detect additional fluorescent signal. Knowing the characteristics of pristine nano sulfur, we were able to detect the in vivo root uptake of nano sulfur. The detection of the nano sulfur within the root cells and within the stomata proved the uptake of the nanoparticles was achieved.

References

Aguilar, A. C. (2019). Nonlinear Optics for Nanoparticle Tracking and Materials Characterization. *Open Access Theses & Dissertations*, *27*.

Aguirre-Olivas, D., Mellado-Villaseñor, G., Sánchez-de-la-Llave, D., & Arrizón, V. (2015). Efficient generation of Hermite–Gauss and Ince–Gauss beams through kinoform phase elements. *Applied Optics*, *54*(28), 8444. https://doi.org/10.1364/ao.54.008444

Bencheikh, A., & Forbes, A. (2020). The non-diffracting nature of truncated Hermite–Gaussian beams. *Journal of the Optical Society of America A*, *37*(11), C1. https://doi.org/10.1364/josaa.385913

Benninger, R. K. P., & Piston, D. W. (2013b). Two-photon excitation microscopy for the study of living cells and tissues. *Current Protocols in Cell Biology*, *Chapter 4*, Unit 4.11.1-24. https://doi.org/10.1002/0471143030.cb0411s59

Broky, J., Siviloglou, G. A., Dogariu, A., & Christodoulides, D. N. (2008). Self-healing properties of optical Airy beams. *Optics Express*, *16*(17), 12880–12891.

Bush, P. G., Wokosin, D. L., & Hall, A. C. (2007). Two-versus one photon excitation laser scanning microscopy: critical importance of excitation wavelength. *Frontiers in Bioscience : A Journal and Virtual Library*, *12*, 2646–2657. https://doi.org/10.2741/2261

Denk, W., Strickler, J. H., & Webb, W. W. (1990). Two-Photon Laser Scanning Fluorescence Microscopy. *Science*, *248*(4951), 73–76. https://doi.org/10.1126/science.2321027

Goeppert Mayer, M. (1931). Disertation Reprint of "Uber Elementarakte mit zwei Quantensprüngen." *Annalen Der Physick9[401] (Annalen Der Physik9[401])*, 273–294.

Goodwin, P. C. (2014). Quantitative deconvolution microscopy. In *Methods in Cell Biology* (Vol. 123, pp. 177–192). Academic Press Inc. https://doi.org/10.1016/B978-0-12-420138-5.00010-0

Guo, C., Liu, W., Hua, X., Li, H., & Jia, S. (2019). Fourier light-field microscopy. *Optics Express*, *27*(18), 25573. https://doi.org/10.1364/OE.27.025573

Gustafsson, M. G. L., Allen, J. R., & Davidson, M. W. (n.d.). *Superresolution Structured Illumination Microscopy*. Zeiss Microscopy Online Campus Website.

Heintzmann, R., & Huser, T. (2017). Super-Resolution Structured Illumination Microscopy. In *Chemical Reviews* (Vol. 117, Issue 23, pp. 13890–13908). American Chemical Society. https://doi.org/10.1021/acs.chemrev.7b00218

Kim, K. (2022). Single-Shot Light-Field Microscopy: An Emerging Tool for 3D Biomedical Imaging. *BioChip Journal*. https://doi.org/10.1007/s13206-022-00077-w

Levoy, M., Ng., R., Adams, A., Footer, M., & Horowitz, M. (2006). Light field microscopy. *ACM Transactions on Graphics*, *25*(3), 924–934.

Levoy M., & Zhang Z. (2009). Recording and controlling the 4D light field in a microscope using microlens arrays. In *Journal of Microscopy* (Vol. 235).

Li, J., Xue, F., Qu, F., Ho, Y.-P., & Blu, T. (2018). On-the-fly estimation of a microscopy point spread function. *Optics Express*, *26*(20), 26120. https://doi.org/10.1364/oe.26.026120

Meena, H. K., & Singh, B. K. (2021). Controlled modulation of optical energy in the high order Hermite-Gaussian laser modes. *Optik*, *232*. https://doi.org/10.1016/j.ijleo.2021.166560

Meena, H. K., & Singh, B. K. (2022). Experimental realization of modulated Hermite–Gaussian laser modes: a maximum number of highly intense lobes. *Journal of the Optical Society of America A*, *39*(11), 2104. https://doi.org/10.1364/josaa.470435

Paez, A. (2019). Non Linear Optics For Materials Fabrication And Medical Instrumentation . *Open Access Theses & Dissertations*, *2885*.

Paschotta, R. (2004). *The RP Photonics Encyclopedia*. RP Photonics.

Siviloglou, G. A., & Christodoulides, D. N. (2007). Accelerating finite energy Airy beams. *Optics Letters*, *32*(8), 979. https://doi.org/10.1364/OL.32.000979

Song, P., Jadan, H. V., Howe, C. L., Foust, A. J., & Dragotti, P. L. (2022). Light-Field Microscopy for Optical Imaging of Neuronal Activity: When Model-Based Methods Meet Data-Driven Approaches. *IEEE Signal Processing Magazine*, *39*(2), 58–72. https://doi.org/10.1109/MSP.2021.3123557

Ugalde-Ontiveros, J. A., Jaimes-Nájera, A., Luo, S., Gómez-Correa, J. E., Pu, J., & Chávez-Cerda, S. (2021). What are the traveling waves composing the Hermite-Gauss beams that make them structured wavefields? *Optics Express*, *29*(18), 29068. https://doi.org/10.1364/oe.424782

Vettenburg, T., Dalgarno, H. I. C., Nylk, J., Coll-Lladó, C., Ferrier, D. E. K., Čižmár, T., Gunn-Moore, F. J., & Dholakia, K. (2014). Light-sheet microscopy using an Airy beam. *Nature Methods*, *11*(5), 541–544. https://doi.org/10.1038/nmeth.2922

Wang, Y., Deng, C., Elmer, W. H., Dimkpa, C. O., Sharma, S., Navarro, G., Wang, Z., Lareau, J., Steven, B. T., Wang, Z., Zhao, L., Li, C., Dhankher, O. P., Gardea-Torresdey, J. L., Xing, B., & White, J. C. (2022). Therapeutic Delivery of Nanoscale Sulfur to Suppress Disease in Tomatoes: In Vitro Imaging and Orthogonal Mechanistic Investigation. *ACS Nano*, *16*(7), 11204–11217. https://doi.org/10.1021/acsnano.2c04073

Vita

Gilberto III Navarro was born and raised in El Paso, Texas. Both of his parents were born in Juarez and became U.S. citizens to live the American dream. While going to high school he attended the UTEP upward bound program, a college readiness program available for low-income families. He graduated in the top 10% from his high school and attended The University of Texas at El Paso where he received his Bachelor of Science in Physics in 2020. While an undergrade he worked as a research assistant in the biophotonics lab with Dr. Chunqaing Li and Dr. Aurelio Paez. Under their mentorship Gilberto was inspired to further pursue a higher education in the field of physics. After completion of his bachelor's degree, he went on to pursue a master's degree in Physics. During his graduate years he continued to work as a research assistant for the biophotonics lab and worked as a teaching assistant for the department of physics. He is now co-author of 3 articles and is now pursuing first author publication.